SAND REPORT

SAND2003-0537
Unlimited Release
Printed February 2003

Effects of Microstructural Variables on the Shock Wave Response of PZT 95/5

R. E. Setchell, B. A. Tuttle, and J. A. Voigt

Prepared by
Sandia National Laboratories
Albuquerque, New Mexico 87185 and Livermore, California 94550

Sandia is a multiprogram laboratory operated by Sandia Corporation,
a Lockheed Martin Company, for the United States Department of Energy's
National Nuclear Security Administration under Contract DE-AC04-94-AL85000.

Issued by Sandia National Laboratories, operated for the United States Department of Energy by Sandia Corporation.

Available to DOE and DOE contractors from
U.S. Department of Energy
Office of Scientific and Technical Information
P.O. Box 62
Oak Ridge, TN 37831

Telephone: (865)576-8401
Facsimile: (865)576-5728
E-Mail: reports@adonis.osti.gov
Online ordering: http://www.doe.gov/bridge

Available to the public from
U.S. Department of Commerce
National Technical Information Service
5285 Port Royal Rd
Springfield, VA 22161

Telephone: (800)553-6847
Facsimile: (703)605-6900
E-Mail: orders@ntis.fedworld.gov
Online order: http://www.ntis.gov/help/ordermethods.asp?loc=7-4-0#online

SAND2003-0537
Unlimited Release
Printed February 2003

Effects of Microstructural Variables on the Shock Wave Response of PZT 95/5

Robert E. Setchell
Nanostructures and Advanced Materials Chemistry Department

Bruce A. Tuttle
Ceramic Materials Department

James A. Voigt
Chemical Synthesis and Nanomaterials Department

Sandia National Laboratories
P.O. Box 5800
Albuquerque, NM 87185-1421

Abstract

The particular lead zirconate/titanate composition PZT 95/5-2Nb was identified many years ago as a promising ferroelectric ceramic for use in shock-driven pulsed power supplies. The bulk density and the corresponding porous microstructure of this material can be varied by adding different types and quantities of organic pore formers prior to bisque firing and sintering. Early studies showed that the porous microstructure could have a significant effect on power supply performance, with only a relatively narrow range of densities providing acceptable shock wave response. However, relatively few studies were performed over the years to characterize the shock response of this material, yielding few insights on how microstructural features actually influence the constitutive mechanical, electrical, and phase-transition properties. The goal of the current work was to address these issues through comparative shock wave experiments on PZT 95/5-2Nb materials having different porous microstructures. A gas-gun facility was used to generate uniaxial-strain shock waves in test materials under carefully controlled impact conditions. Reverse-impact experiments were conducted to obtain basic Hugoniot data, and

transmitted-wave experiments were conducted to examine both constitutive mechanical properties and shock-driven electrical currents. The present work benefited from a recent study in which a baseline material with a particular microstructure had been examined in detail. This study identified a complex mechanical behavior governed by anomalous compressibility and incomplete phase transformation at low shock amplitudes, and by a relatively slow yielding process at high shock amplitudes. Depoling currents are reduced at low shock stresses due to the incomplete transformation, and are reduced further in the presence of a strong electrical field. At high shock stresses, depoling currents are driven by a wave structure governed by the threshold for dynamic yielding. This wave structure is insensitive to the final wave amplitude, resulting in depoling currents that do not increase with shock amplitude for stresses above the yield threshold. In the present study, experiments were conducted under matched experimental conditions to directly compare with the behavior of the baseline material. Only subtle differences were observed in the mechanical and electrical shock responses of common-density materials having different porous microstructures, but large effects were observed when initial density was varied.

Acknowledgments

The shock experiments were skillfully assembled and conducted by D. E. Cox, with facility support from M. U. Anderson. G. A. Samara provided important guidance in the planning and conduct of this study, and E. L. Venturini provided additional material characterizations. This work was supported by Laboratory Directed Research and Development funding.

Contents

Figures

Figures - continued

Tables

1. Introduction

Solid solutions of lead zirconate and lead titanate in different proportions and with various additives have been extensively studied, and many important applications have resulted from their piezoelectric and ferroelectric properties.[1,2] A ferroelectric ceramic exhibits remanent polarization when poled by an applied electric field, and a bound charge is retained. Sudden release of this charge through shock-wave compression was first proposed as a source of pulsed power more than 40 years ago.[3] The available stored energy density is $P_r^2/2\varepsilon$, where P_r is the remanent polarization and ε is the effective permittivity when the bound charge is released.[4] Remanent polarization can be permanently lost during shock compression through ferroelectric domain reorientation or through transformation to a non-ferroelectric phase.[5] A particular composition having a Zr:Ti ratio of 95:5 and modified with 1-2% niobium, denoted by PZT 95/5-2Nb, was identified in early studies as a promising material for this application.[6,7] Processing variables allow the final material to be prepared over a range of densities. At ambient conditions this composition is ferroelectric (FE) with a rhombohedral structure, but is near the boundary for an antiferroelectric (AFE) phase having an orthorhombic structure.[8] At a hydrostatic pressure of approximately 0.3 GPa, the FE-to-AFE phase transformation occurs with a ~0.9% reduction in volume.[9] Shock compression into the AFE phase provides a very fast mechanism for releasing the bound charge.

An early experimental study by Doran[7] used explosive-loading techniques and streak-camera diagnostics to obtain Hugoniot states in unpoled samples having densities that ranged from 7.67 to 7.89 g/cm^3. The position of a cusp in the Hugoniot curve, presumed to be the Hugoniot elastic limit, was found to depend sensitively on initial density. Initial shock-wave studies of poled material used an "axially poled" configuration, where shock propagation occurs along the poling axis.[6] Strong electrical fields are generated in this configuration, and lower-than-expected currents through an external circuit were attributed to shock-induced conductivity.[10] Subsequently, most shock experiments were conducted in a "normally poled" configuration, with shock propagation perpendicular to the poling axis. Electrical fields generated in this configuration can be essentially zero or restricted to some value by choice of a resistive load in an external circuit. Lysne and Percival[11] and Lysne[12] examined the electrical response of poled PZT 95/5-2Nb samples having an initial density of 7.55 g/cm^3 during multi-dimensional shock-

compression experiments. In these studies, depoling currents were measured in an external circuit as a shock wave propagated along a bar of PZT material using an experimental geometry that allowed lateral unloading to occur. Initial shock stresses were estimated to vary from 0.6 to 3.2 GPa, and resistive loads in the external circuit were varied to produce different electric fields during the shock motion. A simple model for the depoling current was used to analyze voltages measured in the external circuit. This model assumed instantaneous and complete depoling at a discontinuous shock front, and the released charge was partitioned between passing through the external circuit and being retained on the sample electrodes to account for the sample capacitance. Different dielectric constants were used for the unshocked and shocked material. This model was fairly successful in predicting measured voltages at shock pressures sufficient to completely depole the sample. To improve comparisons, particularly with experiments having inductive loads, Lysne subsequently added finite resistivity[13] and dielectric relaxation[14] to the analysis. Dick and Vorthman[15] conducted uniaxial-strain shock experiments with PZT 95/5-2Nb samples having densities between 7.29 and 7.32 g/cm^3. A few shock Hugoniot states were measured near 2.0 GPa by impacting unpoled PZT samples into quartz stress gauges. Transmitted wave profiles were recorded at a window interface on the back surface of a PZT sample using laser interferometry. A fixed shock stress of 1.6 GPa was generated in poled and unpoled samples from 2.0 mm to 8.9 mm thick. Currents from the poled samples were measured in an external circuit, and indicated that the phase transformation was incomplete at this stress level. The observed wave profiles showed unsteady wave motion with wave structures dependent on the state of polarization. Of particular significance was one experiment conducted with a large resistive load that resulted in the development of a 20 kV/cm field during the shock motion. In comparison to a similar experiment with a short-circuit load, the high-field case showed a wave profile with a reduced final state, indicating an electromechanical coupling effect.

Over the following twenty years, very few additional studies were made to examine the properties of PZT 95/5-2Nb during shock loading. Chhabildas[16] conducted uniaxial-strain experiments on unpoled PZT 95/5-2Nb samples having a nominal density of 7.30 g/cm^3. Transmitted wave profiles were recorded at a window interface using laser interferometry. Hugoniot states with stresses varying from 0.9 to 4.6 GPa were determined from wave transit times and final velocity values at the window interface. All wave profiles showed extended rise

times, particularly at the lowest and highest stresses. Evidence for the onset of the FE-to-AFE phase transition occurred at approximately 0.5 GPa, and the wave structure above 2.6 GPa showed extended features identified as dynamic pore compaction. A mixed-phase shocked state was indicated at stresses between these levels. Additional experiments to examine shear stresses led Chhabildas to suggest that dynamic yielding could be occurring as well over these stresses. In a follow-on study, Chhabildas et al.[17] conducted recovery experiments on PZT 95/5-2Nb samples shocked to stresses up to 4.6 GPa. Examination of the microstructure in recovered material showed that initially spherical pores introduced during material processing (discussed in Section 2) were progressively deformed as shock stresses increased beyond 1.6 GPa. Extensive fracturing and a high density of dislocations were also evident in material shocked to the higher stresses.

An initial investigation of the effects of changing the porous microstructure in this material was conducted by Storz and Dungan.[18] By adding organic pore formers prior to bisque firing, the final density after sintering could be adjusted. Two types of pore formers, microcrystalline cellulose (MCC) rods and polymethyl methacrylate (PMMA) spheres (described in Section 2), were added in varying amounts to achieve final densities from 7.66 g/cm^3 to less than 7.30 g/cm^3. Testing on these samples included poling characteristics, flexural strength, fracture toughness, hydrostatic depoling, and depoling behavior during explosive-driven shock wave compression. The shock wave experiments were conducted under conditions that resulted in strong electrical fields. This study concluded that an optimum weight percent of added pore former existed for each pore former type, approximately 0.5% and 1.0% for the PMMA spheres and MCC rods, respectively. Flexural strength, fracture toughness, and the percentage of shock experiments that did not experience high-voltage breakdowns were higher at the optimum conditions than for material with no pore formers added. Optimum material made with MCC rods generally performed better during shock testing than the corresponding material made with PMMA spheres. Upper limits to pore former addition were identified to be twice the optimum conditions. When pore formers were added beyond these limits, increasing agglomeration during mixing resulted in large flaws and an open pore structure that rapidly degraded mechanical properties.

In the mid-to-late 1990s, strong interest developed in numerically simulating the operation of pulsed power sources. New experimental data were needed to improve models for dynamic

material properties, leading to a detailed study of a baseline material having a particular microstructure. Extensive uniaxial-strain experiments were conducted to determine Hugoniot states, to examine the constitutive mechanical behavior during shock propagation, and to characterize the depoling kinetics associated with the FE-to-AFE phase transition.[19-23] The collective results identified a complex material behavior governed by anomalous compressibility and incomplete phase transformation at low shock amplitudes, and a slow yielding process at high shock amplitudes. Depoling currents are reduced at low shock stresses due to the incomplete transformation, and are reduced further in the presence of a strong electric field. Experiments using input waves with finite rise times ("ramp waves") showed that transformation kinetics were dependent on the wave structure as well as the final stress. At high shock stresses, depoling currents are driven by a wave structure governed by the threshold for dynamic yielding. This wave structure is insensitive to the final wave amplitude, resulting in depoling currents that do not increase with shock amplitude for stresses above the yield threshold. A number of the baseline material experiments will be discussed in this report in order to provide comparisons with similar experiments using materials having different porous microstructures. Section 2 of this report describes the baseline material and the different PZT 95/5-2Nb materials that were used in the present experiments. Hugoniot states obtained in reverse-impact experiments are summarized in Section 3. The experimental configurations and test conditions used for transmitted-wave experiments are described in Section 4. A summary of the experimental results using the baseline material is given in Section 5. Comparisons between transmitted wave profiles and measured currents are given in Section 6 from experiments that were conducted with common-density materials having different porous microstructures. Similar comparisons are given in Section 7 from experiments that used materials with different initial densities. Conclusions from these comparisons are summarized in the final section.

2. Materials

The PZT 95/5-2Nb materials used in the present study are listed in Table 1. Each material was nominally the same in composition, $Pb_{0.99}Nb_{0.02}(Zr_{0.95},Ti_{0.05})_{0.98}O_3$, but there were differences in the preparation process and in the porous microstructure. The first material, designated MO1, is the baseline material that has been extensively studied. The second column in Table 1 identifies two preparation processes labeled "mixed oxide" and "chemical." In the mixed oxide process,[24] appropriate quantities of ZrO_2, Nb_2O_5, PbO, and TiO_2 powders are intimately mixed, then calcined at approximately 1000 °C to form a solid solution. The calcined powder is wet-milled to an optimum particle size, then oven dried. Small quantities of $PbTiO_3$

Table 1. Materials Examined

Material designations		Preparation	Pore former additive	Density – g/cm^3
This report	Sandia Labs[a]			
MO1	HF453	mixed oxide	0.9 wt % PMMA[b]	7.296 ± 0.023
MO2	HF424	mixed oxide	none	7.659 ± 0.023
CP1	HF631	chemical	1.8 wt % MCC[c]	7.294 ± 0.030
CP2	HF677	chemical	0.45 wt % MCC[c]	7.563 ± 0.019
CP3	HF679	chemical	4.0 wt % MCC[c]	6.943 ± 0.035
CP4[d]	HF963	chemical	0.9 wt % PMMA[e]	7.292 ± 0.020
CP5[d]	HF967	chemical	0.9 wt % PS[f]	7.293 ± 0.021
CP6[d]	HF969	chemical	0.9 wt % PS[g]	7.284 ± 0.014

[a]"high fire" designation used by Sandia National Laboratories
[b]polymethyl methacrylate in the form of spheres 50-100 μm in diameter
[c]microcrystalline cellulose in the form of rods 5-15 μm in diameter and ≥ 20 μm in length
[d]exact composition: $Pb_{0.996}(Zr_{0.953},Ti_{0.047})_{0.982}Nb_{0.018}O_3$ (additional 0.5 mol % Pb used)
[e]polymethyl methacrylate in the form of spheres 14-16 μm in diameter
[f]polystyrene in the form of spheres 77-83 μm in diameter
[g]polystyrene in the form of spheres 135-145 μm in diameter

to refine the stoichiometry are added, together with organic binders to facilitate pressing. At this stage, some weight percent of an organic pore former can be added to control the final fired density. The material is then dry-pressed into billets and bisque fired to remove the organic additives. The billets are sintered at approximately 1350 °C for 6 hours to form the final ceramic. The organic pore former used in the MO1 material is polymethyl methacrylate (PMMA) in the form of spheres having diameters from 50 to 100 μm. The sintered material has distributed spherical pores reflecting the initial size distribution of the PMMA spheres. Approximately 0.9% by weight of these spheres were added for the MO1 material, resulting in a nominal density after sintering of 7.30 g/cm^3. Material heterogeneity extending over sub-millimeter scales occurs in this material due to non-uniform distribution of the spherical voids, and larger voids occur occasionally due to pore-former agglomeration. The MO2 material has no pore former added, and its sintered density is 7.66 g/cm^3. The total void volume fraction (porosity) of the MO1 and MO2 materials is 8.8% and 4.3%, respectively, using 8.00 g/cm^3 for the theoretical maximum density of this composition.

Oxide powders are precipitated from liquid solutions in the more-recent chemical preparation process.[25] These powders are filtered and dried, then calcined at approximately 900 °C for 8 hours. An organic binder and some weight percent of an organic pore former are then added, and pressed billets are bisque fired and sintered under conditions similar to those used in the mixed-oxide process. The pore former used in the first three chemically prepared materials is microcrystalline cellulose (MCC) in the form of rods 5-15 μm in diameter and ≥ 20 μm in length. The sintered material has randomly oriented, distributed voids reflecting the morphology of these rods. Material heterogeneity due to non-uniform pore distribution and pore former agglomeration is less apparent than in the MO1 material. Added weight percents of the pore former are 1.8%, 0.45%, and 4.0%, for the CP1, CP2, and CP3 materials, respectively. The corresponding sintered densities are 7.29 g/cm^3, 7.56 g/cm^3, and 6.94 g/cm^3, and the porosities are 8.8%, 5.5%, and 13.2%. The yield of suitable samples having 13.2% porosity was quite low, and preparation of materials having greater porosity was not attempted. The density of the CP1 material was carefully controlled to match the density of the baseline MO1 material. The densities of the next three materials, designated CP4-CP6, also match the baseline material. Each of these materials was made with spherical pore formers having diameters within a tightly controlled range. Nominal diameters ranged from 15 μm for CP4 to 140 μm for CP6. The grain

size in all of the materials listed in Table 1 is nominally 10 μm, and intergranular voids represent a total porosity of approximately 4%. Figure 1 shows microscope pictures of the last three

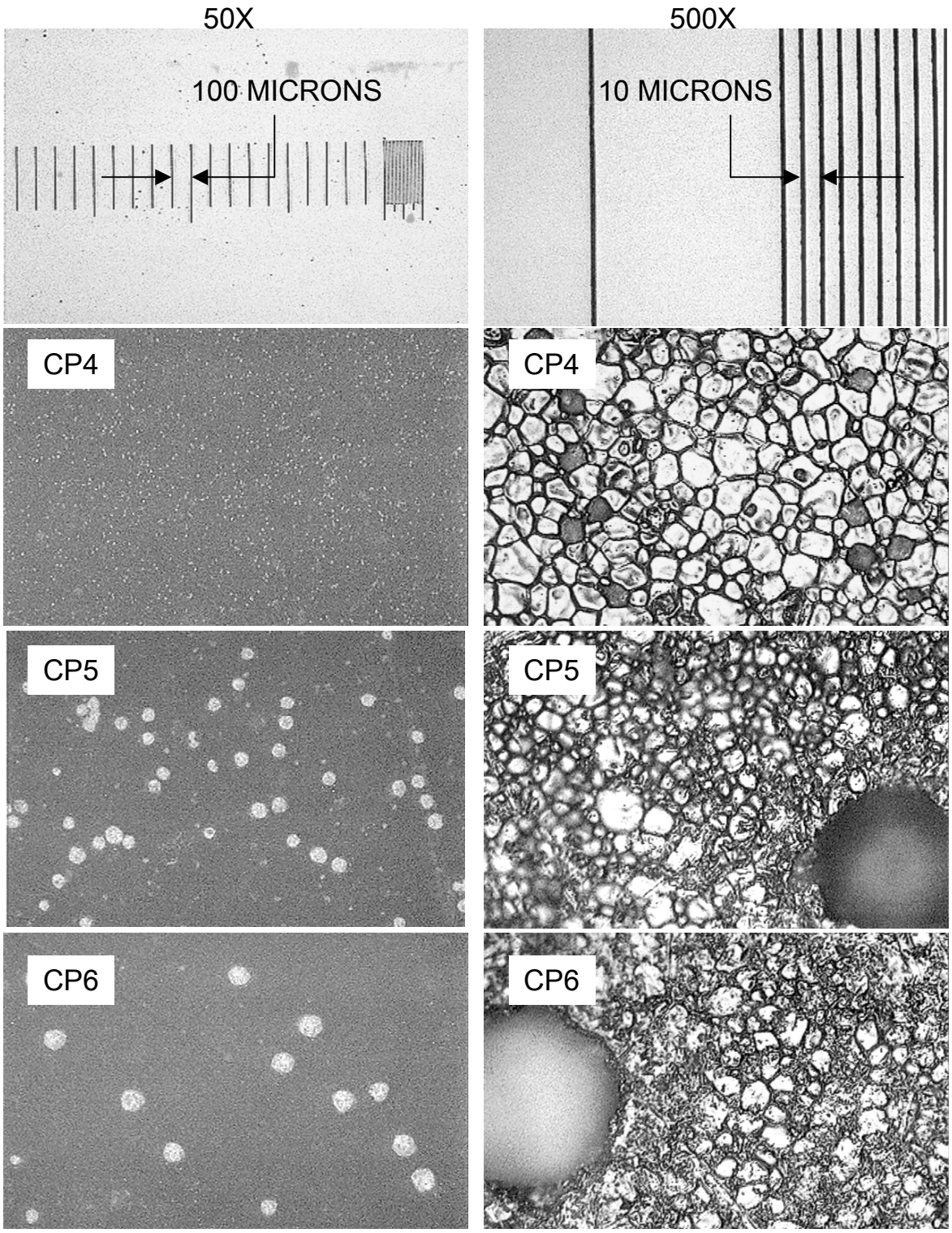

Fig. 1 Microscope photographs of PZT 95/5-2Nb porous microstructure.

materials taken at two different magnifications. Because bulk densities are the same, the average distance between pore-former voids increases as the diameter of the pore former increases. The diameter of the pore former and the nominal grain size are comparable in the CP4 material, resulting in voids that have the shape of missing grains.

Acoustic velocities were measured in unpoled and poled samples from the eight materials. Ultrasonic longitudinal and shear transducers were bonded to sample faces, and velocities determined from pulse-echo, time-of-flight measurements.[26] Figure 2 depicts a typical bar-shaped sample, with the orthogonal axes numbered for convenience. If the material is unpoled,

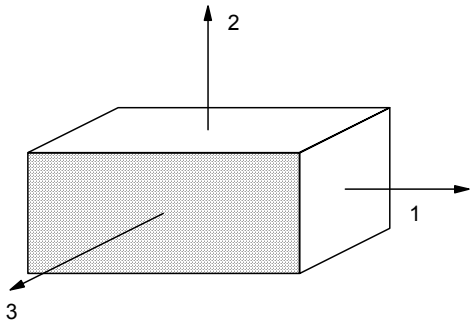

Fig. 2 Orientation of axes in a poled bar of PZT 95/5-2Nb.

properties are isotropic and the axes orientation is not relevant. If two opposing surfaces are electroded and a high field applied to produce a remanent polarization, the material becomes anisotropic. In Fig. 2, the surface in the 1-2 plane is shaded to suggest an electroded surface in a sample that has been poled along the 3 axis. Longitudinal wave motion in such a sample can either be parallel to the poling direction along the 3 axis ("axially poled" motion), or perpendicular to the poling direction along the 1 or 2 axes ("normally poled" motion). Shear wave motion can also be parallel or perpendicular to the poling direction, with normally poled wave propagation having particle motion either parallel or perpendicular to the poling axis. Measured acoustic velocities for the various possible orientations are listed in Table 2. Longitudinal velocities for the unpoled and normally poled cases are expected to be essentially the same, and were not independently measured in all materials. Only unpoled samples of the MO2 material were used in the present study. All velocities increase with increasing density, and longitudinal velocities are highest along the poling axis. Although matched in density, the last three materials (CP4-CP6) had consistently higher acoustic velocities than the MO1 and CP1 materials.

Table 2. Acoustic Velocities

Material	Unpoled	Normally poled		Axially poled
a) Longitudinal wave velocities – km/s:				
MO1	4.163 ± 0.008	4.164 ± 0.013		4.270 ± 0.019
MO2	4.315 ± 0.014	-		-
CP1	-	4.121 ± 0.009		4.196 ± 0.007
CP2	-	4.299 ± 0.015		4.423 ± 0.028
CP3	-	3.847 ± 0.111		4.067 ± 0.083
CP4	4.199 ± 0.010	4.233 ± 0.023		4.315 ± 0.006
CP5	4.217 ± 0.0.007	4.233 ± 0.009		4.325 ± 0.007
CP6	4.222 ± 0.024	4.234 ± 0.011		4.321 ± 0.007
b) Shear wave velocities – km/s:		parallel[a]	perpendicular[b]	
MO1	2.518 ± 0.006	2.557 ± 0.009	2.468 ± 0.008	2.409 ± 0.011
MO2	2.609 ± 0.008	-	-	-
CP1	-	2.525 ± 0.006	2.451 ± 0.003	2.380 ± 0.008
CP2	-	2.643 ± 0.009	2.541 ± 0.008	2.475 ± 0.007
CP3	-	2.384 ± 0.014	2.328 ± 0.046	2.235 ± 0.039
CP4	2.556 ± 0.006	2.586 ± 0.007	2.511 ± 0.004	2.459 ± 0.004
CP5	2.562 ± 0.006	2.590 ± 0.008	2.518 ± 0.008	2.459 ± 0.003
CP6	2.555 ± 0.004	2.581 ± 0.004	2.509 ± 0.004	2.462 ± 0.003

[a]particle motion parallel to poling axis
[b]particle motion perpendicular to poling axis

Some additional information on phase transition and phase diagram characteristics of PZT 95/5-2Nb materials having different porous microstructures can be found in Appendix A.

3. Hugoniot States

A fundamental characterization of how a material responds under shock compression is the determination of Hugoniot states over some range of shock conditions.[27] Hugoniot curves identify the thermodynamic states that can be achieved in a material through adiabatic compression by a steady shock wave. Mass, momentum and energy conservation across the shock wave link the thermodynamic variables to the wave and particle velocities associated with the wave motion. If a material has constitutive properties that result in unsteady shock motion, methods that utilize transmitted-wave measurements for determining Hugoniot states may not be suitable. A relatively unambiguous technique for arbitrary materials is to conduct "reverse impact" experiments, in which a test material is accelerated to a measured velocity and then impacted into a reference material having well-established Hugoniot properties. Planar shock waves are generated in both materials at impact, with axial stress and particle velocity continuous at the impact interface. Measurement of either the axial stress or the particle velocity of this interface provides a stress-velocity Hugoniot state for the test material. In the present study, laser interferometry is used to measure the impact interface velocity when thin PZT samples are accelerated into fused-silica windows. Sufficient reverse-impact experiments were conducted previously with the baseline MO1 material to establish a fairly complete Hugoniot curve over a 1.0-5.0 GPa stress range of interest. In the present study, limited experiments were conducted with other PZT materials to provide basic comparisons.

Experiments were conducted on a compressed-gas gun capable of achieving impact velocities from 0.03 to 1.3 km/s, which is a sufficient range for generating all shock conditions of practical interest in PZT 95/5-2Nb. The barrel has a diameter of 63.5 mm and a length of 25 m, although projectiles are initially positioned closer to the target to achieve good reproducibility for impact velocities below 0.2 km/s. Four electrical contact pins spaced within the final 9 cm of the barrel are used to measure the impact velocity to within approximately 0.2%. The primary instrumentation for these experiments is a laser velocity interferometer, commonly known as a VISAR,[28] which measures the particle velocity history at a reflecting interface between a sample and an attached window. Details on the design and performance of the VISAR system used in the present study have been reported previously.[29]

Figure 3 shows the experimental configuration used for generating data on Hugoniot states. The projectile facing consisted of a sample of unpoled PZT 95/5-2Nb mounted on a layer of 0.27

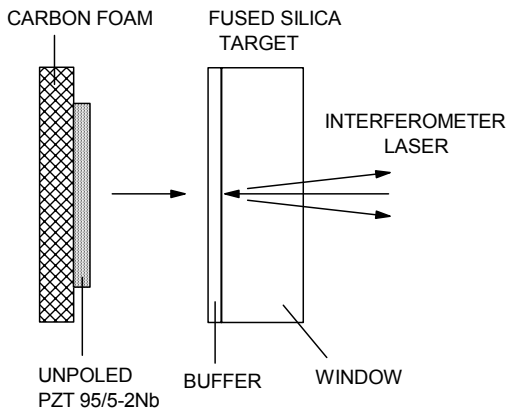

Fig. 3 Experimental configuration for reverse-impact experiments.

g/cm^3 carbon foam. The PZT samples were either discs with 25-mm diameters or squares with 25-mm edges, with sample surfaces flat and parallel to within 0.025 mm. Sample thickness was typically 2.0 mm. The target assembly contained fused-silica buffer and window pieces that were nominally 1.6 mm and 12.7 mm in thickness, respectively, and 50.8 mm in diameter. Prior to bonding these two pieces with thin-film epoxy, the window surface was roughened to become somewhat diffusely reflecting, then coated with approximately 200 nm of vapor-deposited aluminum. The VISAR instrumentation recorded the shock wave profile at the interface between the buffer and window pieces. Following a small correction due to refractive index changes in the window,[30] the corresponding wave profiles at the impact interface are then calculated using the well-known dynamic properties of fused silica.[31] Allowing the waves to propagate through a finite distance of fused silica, rather than recording the motion of the impact interface directly, reduces the sensitivity of the measured profiles to local heterogeneities in the PZT samples. Part tolerances, projectile and target assembly procedures, and target alignment procedures resulted in near-planar impacts with tilt angles less than 0.5 mrad.

Table 3 lists the impact conditions, measured particle velocities, and calculated Hugoniot conditions for the reverse-impact experiments that were conducted. The individual experiment numbers identify the PZT material and the reverse-impact configuration. The first nine experiments listed were conducted previously using the MO1 baseline material, and spanned a stress range from 0.9 to 5.2 GPa. Figure 4 shows the stress-velocity Hugoniot points obtained in these experiments. The linear "elastic" MO1 curve simply reflects the initial density and the measured longitudinal sound speed (Tables 1 and 2). A polynomial fit to the measured MO1

Table 3. Experimental Conditions and Measured Velocities in Reverse-Impact Experiments

Experiment number	Impact velocity – km/s	Measured window velocity – km/s	Hugoniot conditions stress – GPa	Hugoniot conditions velocity – km/s	Hugoniot conditions strain[b]
MO1RI1	0.1118	0.0726	0.924	0.0392	0.0121
MO1RI2	0.1763	0.1187	1.484	0.0576	0.0163
MO1RI3	0.2296	0.1567	1.931	0.0729	0.0200
MO1RI4	0.2955	0.2006	2.436	0.0949	0.0269
MO1RI5	0.3517	0.2352	2.828	0.1165	0.0351
MO1RI6	0.4175	0.2708	3.225	0.1467	0.0486
MO1RI7	0.5031	0.3183	3.751	0.1848	0.0663
MO1RI8	0.6067	0.3816	4.450	0.2251	0.0829
MO1RI9[a]	0.7183	0.4513	5.223	0.2670	0.0993
MO2RI1	0.4059	0.2948	3.492	0.1111	0.0264
MO2RI2	0.6227	0.4462	5.166	0.1765	0.0451
MO2RI3	0.8811	0.6189	7.130	0.2622	0.0721
CP1RI1	0.6194	0.3946	4.594	0.2248	0.0804
CP2RI1	0.6214	0.4286	4.970	0.1928	0.0557
CP3RI1	0.6174	0.3437	4.031	0.2737	0.1321

[a]impactor backed by sapphire (no release wave generated)
[b]ratio of particle velocity to shock velocity, calculated using steady-wave jump conditions[27]

points which preserves the initial elastic slope is also shown. A high-order polynomial is required to accurately account for the multiple changes in curvature that are apparent. Interpretation of the features shown by this curve are guided by the earlier study of Chhabildas.[16] The curve shows a negative curvature below 0.5 GPa, corresponding to anomalous compressibility. This would result in an unsteady "ramp" wave at the foot of a propagating wave, as will be shown in transmitted-wave experiments. The curvature reverses with the onset of the FE-to-AFE phase transformation, but is clearly negative again at stresses above 2.0 GPa where dynamic yielding occurs. Measurements of depoling currents from normally poled MO1 materials (Section 5) confirm that a mixed-phase state is produced within the time scales of

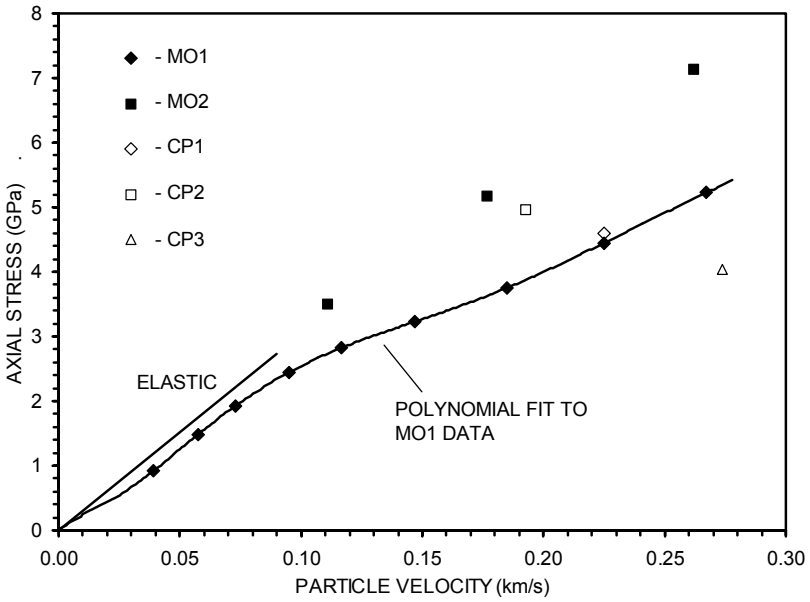

Fig. 4 Hugoniot states for various test materials.

the shock experiments until the shock stress approaches 2.0 GPa. The negative curvature from 2.0 GPa to approximately 4.0 GPa would again correspond to unsteady wave motion, as will also be shown in transmitted-wave experiments. At higher stresses the Hugoniot fit shows little curvature.

Comparisons between the MO1 Hugoniot curve and limited data obtained with other materials are also shown in Fig. 4. These results indicate that Hugoniot curves for PZT 95/5-2Nb are quite sensitive to differences in initial density. The CP1 measurement is slightly higher than the MO1 curve, although the particular CP1 sample used in this experiment had the highest density (7.324 g/cm^3) of the CP1 sample lot. Transmitted-wave experiments also indicate that, within experimental accuracy, the polynomial fit for MO1 material is suitable for the similar-density CP1 material. The data points for the high-density MO2 material appear to nearly fall on a linear curve, although additional points would be necessary to establish the extent of curve inflections resulting from dynamic yielding.

4. Configurations and Conditions for Transmitted-Wave Experiments

To study the dynamic stress-strain behavior of a material under shock compression, the evolution of shock wave profiles can be examined while varying propagation distance and initial shock amplitude. Comparisons between measured profiles and profiles predicted by numerical simulations are essential for developing and assessing the dynamic material models used in the simulations. When transmitted-wave experiments are conducted on poled materials, measured depoling currents provide a means for assessing models for transformation kinetics and dielectric properties. Figure 5 shows an experimental configuration used for many of the transmitted-wave

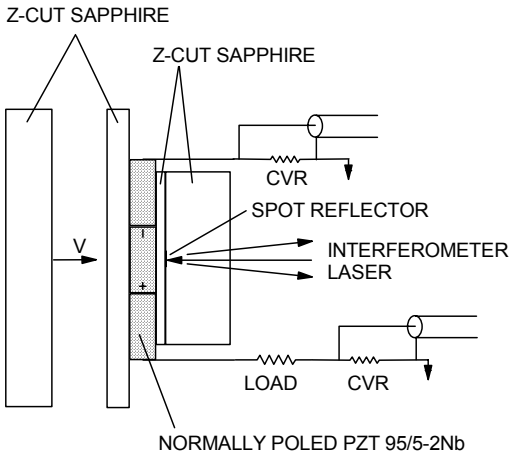

Fig. 5 Configuration for transmitted wave experiments on normally poled samples.

experiments, in which wave propagation in poled material occurs in a direction normal to the poling axis. The impactor mounted on the projectile facing was a disc of Z-cut sapphire, and the target assembly consisted of a sapphire target facing, three bars of poled PZT 95/5-2Nb, and a sapphire buffer and window pair. The PZT bars were nominally 4 mm in the direction of shock propagation, 10 mm in the direction of polarization, and 28 mm long (out of the plane of Fig. 5). For each bar, silver electrodes were deposited on both 4mm by 28 mm faces, and a 15 kV/cm poling field was applied at 100 °C to achieve a nominal remanent polarization of 30 $\mu C/cm^2$. The outer two bars then had conducting layers deposited on all remaining faces so that their entire external surface was electrically shorted. These bars provided a boundary matched in shock impedance for the active center bar, as well as the means for linking the center bar to the circuitry shown in Fig. 5. With this arrangement, only ~14% of the center bar volume

experiences some degree of lateral unloading during shock wave transit. The circuitry was used to observe depoling currents generated by the shock-driven FE-to-AFE phase transition. A load resistor of 10Ω or less was used for depoling under essentially short-circuit conditions, and larger resistors were used to allow significant electrical fields to develop during the shock motion.

The target elements were encapsulated in a target fixture using an alumina-loaded epoxy. To minimize conducting surfaces within regions where high fields could develop, the reflecting interface for the VISAR instrumentation was confined to a 0.04 cm^2 spot. Recorded VISAR signals require a significant correction to account for refractive-index changes in the sapphire window, and the results of a recent study on sapphire[29] were used for this correction. Because the dynamic stress-strain behavior of sapphire is nearly linearly elastic over the range of stresses produced in these experiments,[32] the waveform at the PZT/buffer interface is given very accurately by the waveform recorded at the buffer/window interface.

Sapphire was chosen for the buffer/window assembly because it is the only known window material that has been well-characterized for VISAR applications[29] that also has a higher shock impedance than the PZT ceramics. A transmitted compressive wave reaching the PZT/buffer interface will result in an additional compressive wave reflected back into the PZT. In a material with inelastic behavior, this wave interaction can be more accurately analyzed using an established Hugoniot curve than can an interaction which produces a reflected rarefaction wave. Wave speeds in sapphire are very high,[32] however, and this limits the available time for accurately recording a wave profile. In most experiments, useful recording time was not limited by the arrival of lateral unloading waves at the VISAR spot reflector, but rather by the arrival of the transmitted wave at the back surface of the window. The refractive-index changes associated with the wave reflection at this free surface result in the generation of VISAR interference fringes unrelated to possible velocity changes occurring at the spot reflector.[29] Although it is possible to correct the measured VISAR signals for these effects with some difficulty, this was not done in the present study since lateral unloading waves typically arrived at the VISAR spot shortly thereafter.

Table 4 provides descriptions of other configurations used for some transmitted-wave experiments. The configuration identified as "A" is that shown in Fig. 5. Configuration "B" was used for experiments with unpoled PZT samples. No target facing was used in this case, and the

Table 4. Configurations for Transmitted Wave Experiments[a]

Configuration	Impactor	Target facing	Buffer	Window
A	sapphire[b]	sapphire	sapphire	sapphire
	12.7 X 50.8	3.2 X 50.8	1.6 X 31.8	12.7 X 38.1
B	fused silica[c]	none	sapphire	sapphire
	6.47 X 50.8		1.6 X 31.8	12.7 X 38.1
C	ALOX[d]	ALOX	sapphire	sapphire
	12.7 X 50.8	3.2 X 50.8	1.6 X 31.8	12.7 X 38.1

[a]all elements are discs; the first dimension is thickness (mm), and the second is diameter (mm)
[b]Z-cut sapphire from Meller Optics, Inc., Providence, RI.
[c]Dynasil 1000 synthetic fused silica from Dynasil Corp., Berlin, NJ.
[d]see text for ALOX description

PZT samples were typically circular discs having a nominal thickness of 4.0 mm and a diameter of 25.4 mm. Configuration "C" was used for normally poled samples in the same manner as configuration "A," except that the sapphire impactor and target facing were replaced by discs of alumina-filled epoxy, or ALOX. The particular ALOX that was used has 42% by weight alumina powder added to Shell Epon 828/Z epoxy, and has been well-characterized in shock experiments.[33] The purpose of conducting experiments in this configuration is to introduce a structured wave having a finite rise time into a PZT sample, rather than a sharp shock jump as produced using sapphire elements. This provides an additional means for investigating rate dependencies in material behavior. Figure 6 shows the differences in input waves for these two configurations under three different impact conditions that were used in the present study to produce 0.9, 2.5 and 4.6 GPa peak stresses in baseline-density samples. The ALOX profiles were calculated from profiles measured at an ALOX/window interface in configuration "C" experiments with no PZT sample present. The strongly viscous behavior of ALOX results in a transmitted wave having an extended rise time that depends inversely on the wave amplitude.

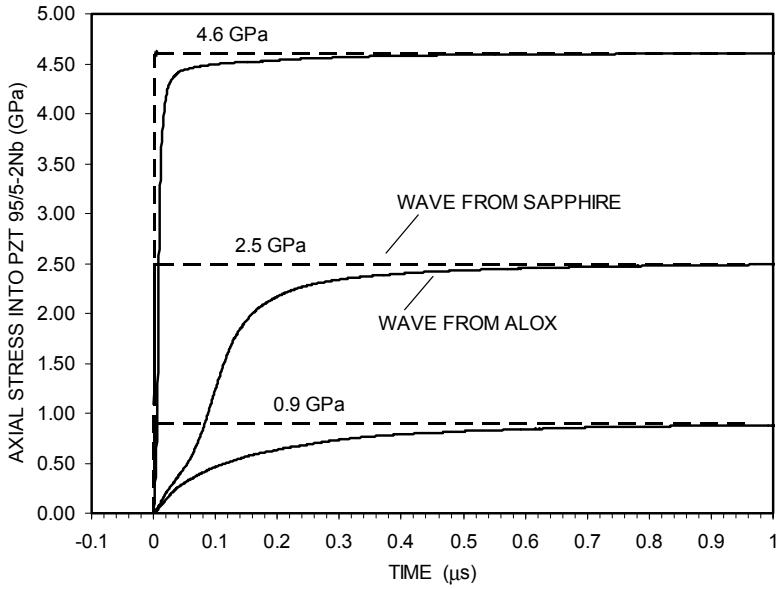

Fig. 6. Input wave profiles generated in either sapphire (shock input) or ALOX (ramp input).

Table 5 lists the specific configuration, poling condition and resistive load, impact velocity, and calculated peak axial stress for each of the transmitted-wave experiments that were conducted. The individual experiment numbers identify the PZT material and the general transmitted-wave configuration. Most of the MO1 experiments listed were conducted previously, and will be used to provide comparisons with the current data. A polynomial fit to the MO1 Hugoniot data shown in Fig. 4, and the well-established Hugoniot properties for sapphire[32] and fused silica,[31] were used to predict the peak axial stress in the PZT samples for experiments using the common-density MO1, CP1, and CP4-CP6 materials. The Hugoniot data obtained for unpoled MO1 was assumed to apply to normally poled material. A simpler fit to the MO2 Hugoniot data (Fig. 4) was used for the MO2 experiments, and values for the CP2 and CP3 experiments were estimated from the results of reverse-impact experiments using these materials.

Table 5. Experimental Conditions for Transmitted-Wave Experiments

Experiment number	Poling/Load	Configuration[a]	Impact velocity – km/s	Peak predicted axial stress - GPa
MO1TW1	NP/10Ω	A	0.0598	0.92
MO1TW2	NP/10Ω	A	0.0961	1.58

Table 5 (continued). Experimental Conditions For Transmitted-Wave Experiments

Experiment number	Poling/Load	Configuration[a]	Impact velocity – km/s	Peak predicted axial stress - GPa
MO1TW3	NP/10Ω	A	0.1080	1.79
MO1TW4	NP/10Ω	A	0.1527	2.49
MO1TW5	NP/10Ω	A	0.2221	3.26
MO1TW6	NP/10Ω	A	0.2781	3.86
MO1TW7	NP/10Ω	A	0.3286	4.50
MO1TW8	NP/10Ω	A	0.0456	0.68
MO1TW9	NP/10Ω	A	0.0403	0.59
MO1TW10	NP/10Ω	C	0.4044	2.52
MO1TW11	NP/375Ω	A	0.1510	2.46
MO1TW12	NP/750Ω	A	0.1496	2.44
MO1TW13	NP/1150Ω	A	0.1542	2.51
MO1TW14	NP/1150Ω	A	0.0973	1.60
MO1TW15	NP/1150Ω	A	0.0599	0.92
MO1TW16	NP/1150Ω	C	0.7365	4.61
MO1TW17	NP/1150Ω	C	0.4021	2.51
MO2TW1	UP	B	0.6213	5.17
CP1TW1	NP/10Ω	A	0.0622	0.97
CP1TW2	NP/10Ω	C	0.1579	0.90
CP1TW3	NP/1150Ω	C	0.7429	4.66
CP1TW4	NP/10Ω	C	0.4076	2.54
CP1TW5	NP/1150Ω	A	0.0595	0.92
CP1TW6	NP/1150Ω	C	0.4020	2.51
CP1TW7	UP	B	0.6180	4.53
CP2TW1	NP/10Ω	C	0.4047	2.6-2.7[b]
CP2TW2	NP/1150Ω	C	0.4048	2.6-2.7[b]

Table 5 (continued). Experimental Conditions For Transmitted-Wave Experiments

Experiment number	Poling/Load	Configuration[a]	Impact velocity – km/s	Peak predicted axial stress - GPa
CP2TW3	UP	B	0.6188	4.95
CP3TW1	NP/10Ω	C	0.4055	2.3-2.4[b]
CP3TW2	UP	B	0.6201	4.05
CP4TW1	NP/10Ω	A	0.3255	4.46
CP5TW1	NP/10Ω	A	0.3256	4.46
CP5TW2	NP/1150Ω	A	0.1560	2.53
CP6TW1	NP/10Ω	A	0.3276	4.49

[a]Table IV
[b]estimate (insufficient Hugoniot data)

5. General Features from Baseline Material Experiments

Figure 7 shows the general features of transmitted wave profiles in the MO1 baseline material. All of these experiments were in the "A" configuration (Fig. 5), with 4.0-mm-thick, normally poled samples under short-circuit loading. Impact velocities ranged from 0.06 to 0.33 km/s, resulting in predicted peak stresses from 0.9 to 4.5 GPa. In every case, an initially sharp input shock (Fig. 6) has evolved into a structured waveform. To within the limited accuracy of current wave-transit timing on the gas-gun facility (±0.035 μs), the "toe" of each wave propagated through the corresponding sample at the longitudinal wave speed (Table 2). For simplicity, all wave profiles are plotted from the time of wave arrival. Every profile shows an

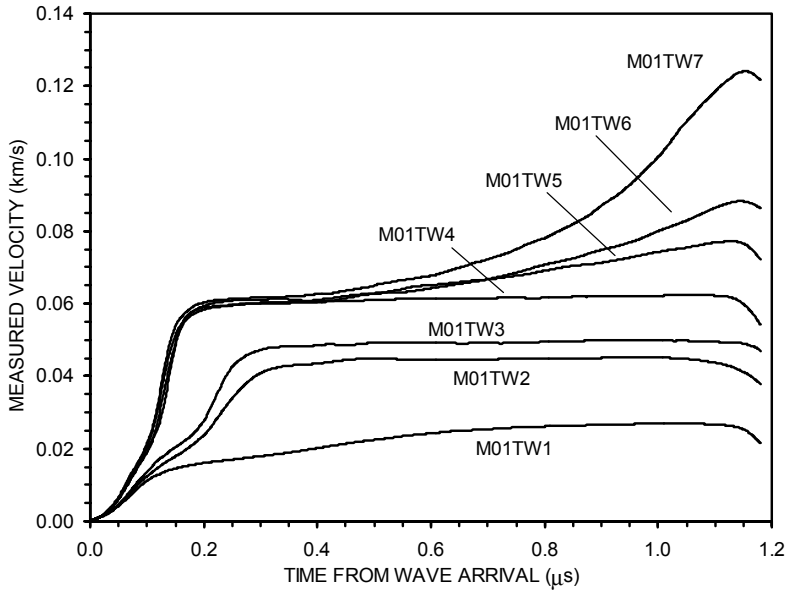

Fig. 7 Transmitted wave profiles in normally poled, short-circuited MO1 samples for different shock input conditions.

initial "ramp" feature consistent with the initial region of negative curvature in the Hugoniot curve (Fig. 4). A possible mechanism for this feature was discussed by Fritz,[9] who conducted quasi-static, uniaxial compression tests of unpoled and poled material similar to MO1. He observed charge release and deviations from linear elastic behavior before the onset of the phase transition, which he interpreted in terms of domain reorientation (switching) processes. The crystalline unit cell is elongated along the polarization axis, and an applied stress can be partially relieved if domains with a polar axis close to the stress direction can switch to a configuration

with the axis away from the stress direction. This would result in larger-than-linear compressive strains in the direction of applied stress. During uniaxial-strain shock propagation, domain reorientation processes could result in anomalous (increasing) compressibility, leading to negative curvature in the Hugoniot curve and the corresponding "ramp" feature. However, the resulting lateral strains would have to be accommodated by reductions in the local porosity.

The lowest profile in Fig. 7 (0.92 GPa) shows an extended structure requiring ~ 0.8 μs to rise to a final state. The next two profiles (1.58 and 1.79 GPa) correspond to increasing impact velocities, and a distinct two-wave structure can be seen during the ~ 0.3 μs rise times. The initial break from the rise of the first wave occurs at a measured interface velocity of approximately 0.015 km/s. This value corresponds to an axial stress of 0.5 GPa in the PZT wave prior to the window interaction (using the MO1 Hugoniot curve and the sapphire Hugoniot in an impedance-matching calculation). This break can be interpreted as the onset of the FE-to-AFE phase transition under these experimental conditions. The fourth profile (2.49 GPa) has a rise time less than 0.2 μs, and represents a limiting case for the profiles shown in Fig. 7. As impact velocity is increased further, the wave structure reflecting the phase transition is insensitive to the final wave amplitude. In addition, a consistent plateau appears that is also insensitive to the final amplitude. An average value for the measured interface velocity at this plateau is 0.061 km/s, which corresponds to an axial stress of 2.2 GPa in the PZT wave prior to the window interaction. This plateau can be interpreted as the onset of dynamic yielding in the material, which is generally referred to as the Hugoniot elastic limit. Use of this terminology may be questionable, however, if the material displays inelastic behavior at lower stresses. Since the microstructure in MO1 material has large spherical voids (Section 2), identifying this plateau with the onset of a pore compaction mechanism[16] seems reasonable. The exact nature of the yielding mechanism in the MO1 material and in the other PZT materials is not known, however, and for present purposes the plateau and subsequent wave structure will simply be associated with an unspecified yielding process. At the highest impact velocities the measured velocity slowly rises from the plateau value towards the final state that would be predicted by the Hugoniot curve. Useful VISAR recording time in this experimental configuration is approximately 1.1 μs after wave arrival, and these profiles do not reach the predicted states within that time. The highest profile comes closest to its predicted final state, indicating that the rise time for this part of the wave structure decreases as final wave amplitudes increase.

Figure 8 shows depoling currents generated under short-circuit conditions during shock propagation through normally poled MO1 samples. Five of these cases correspond to wave profiles shown in Fig. 7, and two additional cases are shown corresponding to very low impact velocities. The start of each current profile corresponds to the entry of the sharp initial shock into the sample, whereas the final portion of current profile corresponds to the structured waveforms (Fig. 7) arriving and interacting at the back sapphire interface. The time T* in Fig. 8

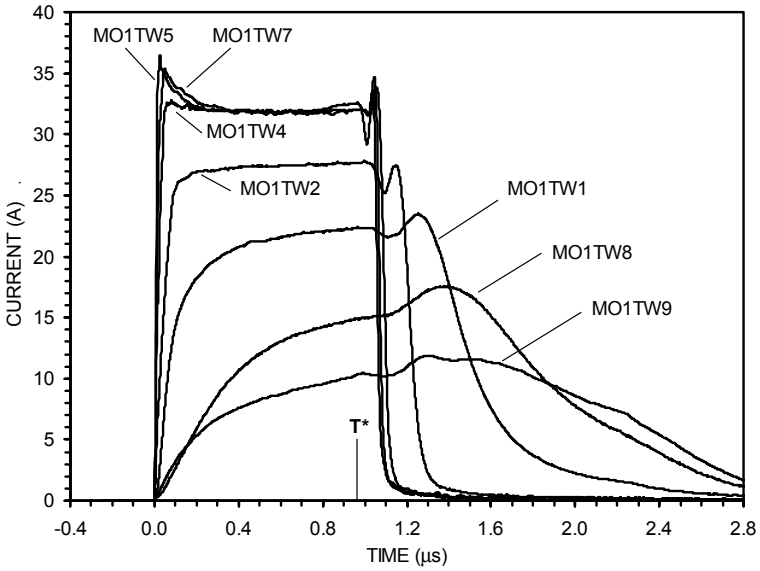

Fig. 8 Short-circuit currents generated from different shock inputs into MO1 samples. T indicates the time when the wave "toe" reaches the sample/window interface.*

indicates the time when the wave "toe" reaches this interface. At a shock stress of 2.49 GPa (TW4), a very flat current profile is observed, with a fairly abrupt initial rise and subsequent fall. The level of this current is accurately predicted by the simple model:[11]

$$I_{sc} = U_S \cdot P_r \cdot L \qquad (1)$$

where the short-circuit current I_{sc} is given by the product of the shock velocity U_S, the remanent polarization P_r, and the electrode dimension L that is perpendicular to the shock direction. This expression corresponds to very rapid, complete depolarization by a shock discontinuity. For initial shock pressures well above the threshold for dynamic yielding (MO5, MO7), a transient overshoot is followed by a steady current at the same level as the TW4 case. A corresponding overshoot is seen in VISAR profiles from reverse-impact experiments at these shock pressures,[23] indicating a fast relaxation at the initially shocked surface from an instantaneous higher-stress

state towards a lower-stress equilibrium state. The fact that the steady current level is the same in these cases indicates that only the part of the wave structure up to the plateau condition (Fig. 7) is responsible for depoling the material. Thus, with the exception of the initial overshoot, depoling currents are independent of the shock amplitude for amplitudes above the threshold for dynamic yielding.

The current profiles for lower shock amplitudes show increasing rise times and decreasing peak values as amplitudes decrease. These features indicate retarded transformation kinetics and a reduced degree of transformation, resulting in a significant fraction of the original bound charge still remaining when the wave reaches the back sapphire interface. Four of the cases in Fig. 8, corresponding to shock amplitudes of 1.58 GPa (TW2) or lower, show these effects. As shock stresses decrease, the reduced depoling currents extend significantly in time. The low-amplitude waves have extended structures (Fig. 7), requiring more time beyond T* for material near the end of the sample to be compressed. In addition, the higher shock impedance of sapphire results in a stronger compressive wave reflected back into the sample, and this wave continues to depole the sample much later in time. The assumptions used for the simple current model given by Eq. (1) do not hold for these shock conditions, and accurate prediction of the measured currents could require a model incorporating retarded and incomplete transformation kinetics linked to the actual wave structures.

Figures 9 and 10 show comparisons between shock input and ramp input cases for peak stress conditions of 2.5 GPa and 0.9 GPa. Because few baseline material experiments were performed under ramp input conditions, the 0.9 GPa cases shown were conducted using the common-density CP1 material. As would be expected from the input wave profiles shown in Fig. 6, the differences from the two input conditions are largest for the lowest peak stress condition. The top curve in each pair corresponds to the shock input case. The 2.5 GPa transmitted waves in Fig. 9 show a more extended structure and a reduced plateau level resulting from the ramp input. For the 0.9 GPa transmitted waves, twice the measured velocities are plotted to facilitate comparisons. Differences are more extreme in this case, with the ramp-input profile never reaching a matching final state within the available test time. In Fig. 10, the corresponding short-circuit currents show small differences in the 2.5 GPa case and significant differences in the 0.9 GPa case. The currents are plotted relative to the time the input wave enters the sample, and the currents from ramp inputs appear to start after this time. Because the ramp input rises

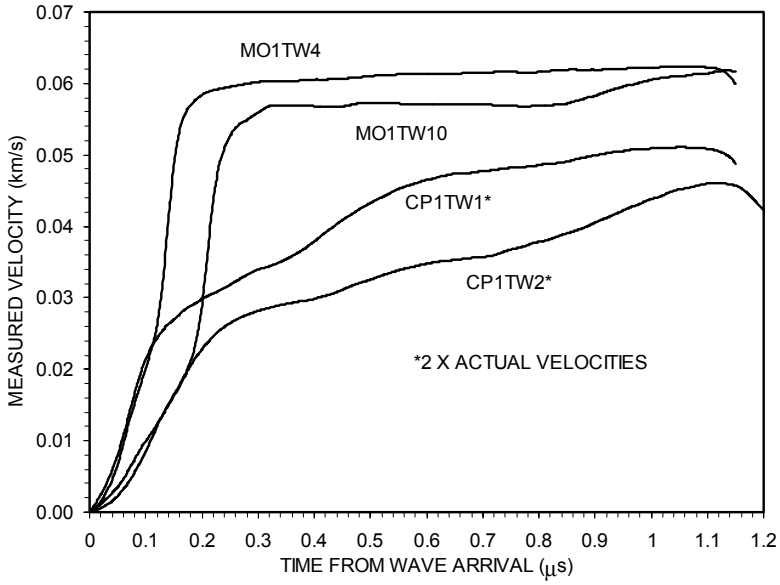

Fig. 9 Effects of input wave type on transmitted wave profiles.

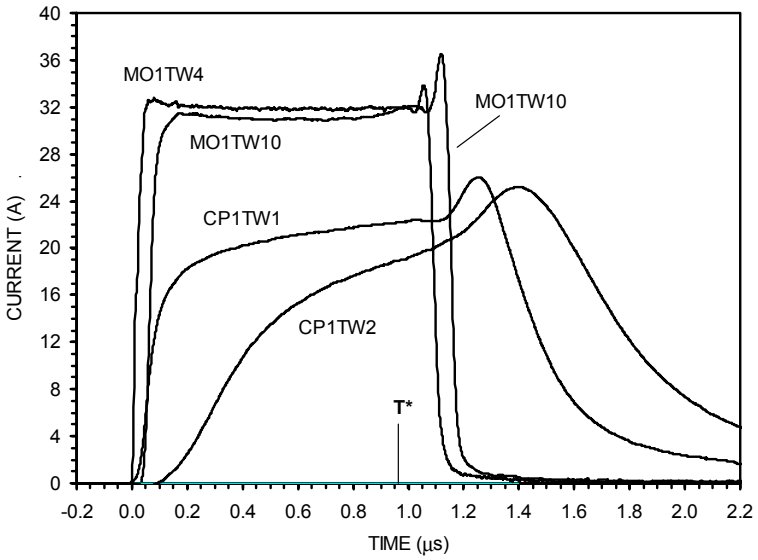

Fig. 10 Effects on input wave type on short-circuit currents.

slowly, the initial response of the sample is piezoelectric, and a weak negative current is recorded until stresses are high enough to start the depoling process.

An important question for PZT 95/5-2Nb applications is the extent to which the constitutive mechanical properties can be influenced by the presence of a strong electric field. Such fields are generated directly by shock-driven depoling in axially poled configurations,[6,34] and can be

generated in normally poled configurations if the depoling current is directed through a high-resistance load.[11] Dick and Vorthman[15] had one experimental result with a normally poled material similar to MO1 in which a 20 kV/cm field was produced during the transit of a 1.6 GPa shock. In comparison to a similar experiment with a short-circuit load, the high-field case showed a wave profile with a reduced final state, suggesting an electromechanical effect that made the material appear "stiffer" (as if the Hugoniot curve were steeper). To explore this issue in the baseline material work, a number of normally poled experiments (configuration "A") were conducted with increasing values of load resistance. Impact conditions were chosen to produce a 2.5 GPa final stress. The measured wave profiles from these experiments are shown in Fig. 11.

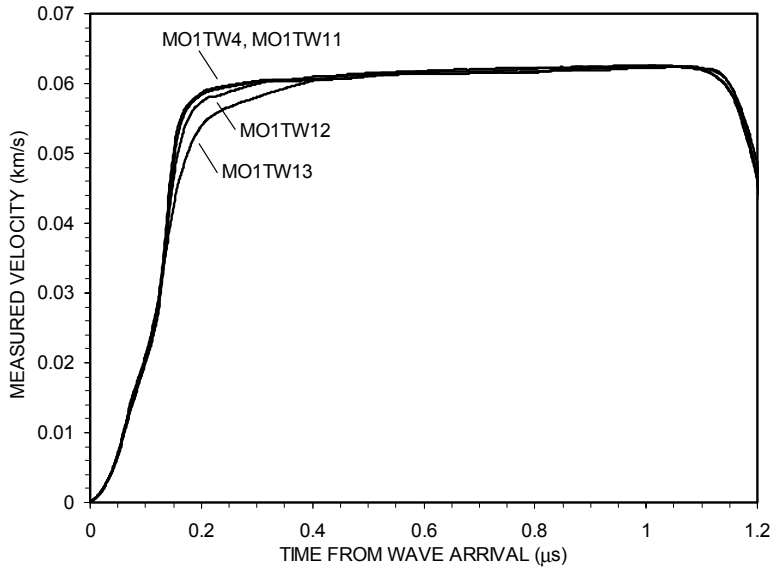

Fig. 11 Field effects on transmitted wave profiles for 2.5 GPa shock inputs.

The load resistances were 10Ω, 375Ω, 750Ω, and 1150Ω for the TW4, TW11, TW12, and TW13 cases, respectively. Corresponding peak fields were 0.3 kV/cm, 12.0 kV/cm, 23.8 kV/cm, and 36.8 kV/cm, as determined from measured currents. The field is developed during shock transit as the depoling current is divided between passing through the load resistor and charging the capacitance of the PZT element.[11] Consequently, it takes an increasing fraction of the total shock transit time for the peak field to be established as the load resistor is increased. For the highest field developed, about half of the transit time through the 4.0-mm-thick sample was required (shown in a subsequent figure). The profiles in Fig. 11 have been scaled slightly to account for the small differences in impact velocity (Table 5). Clearly, no change in the final

state can be seen under these conditions. The only field effect on these transmitted waveforms appears to be an increase in the time required to reach the final state with increasing field strength. This effect may have been amplified in the experiment of Dick and Vorthman, in which the propagation distance was considerably longer (8.2 mm).

Figure 12 shows field effects on measured currents for 2.5 GPa, 1.6 GPa, and 0.9 GPa shock inputs. The top curve in each pair corresponds to a 10Ω load resistor, and the matching high-field curves were obtained with 1150Ω loads. The high-load currents rise with a characteristic

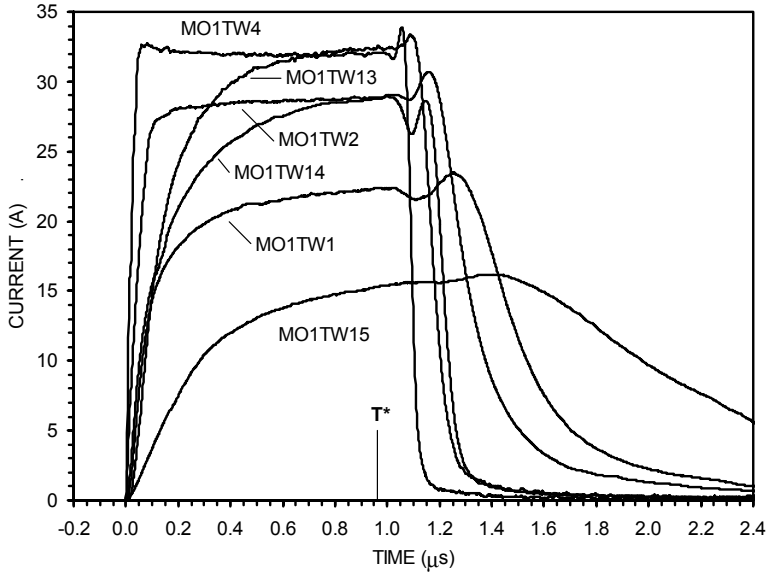

Fig. 12 Field effects on currents generated from shock inputs.

"RC" time constant resulting from the sample capacitance. Using Eq. (1) for the depoling current, Lysne and Percival[11] and Lysne[12] used similar high-field current histories to examine dielectric properties during shock propagation. In the 2.5 GPa and 1.6 GPa cases, currents through the load circuit eventually reach short-circuit values. Significantly reduced currents are recorded in the high-load 0.9 GPa case, however, indicating that the transformation kinetics are further retarded by the presence of the field. The transmitted wave profiles for the 1.6 GPa and 0.9 GPa experiments are shown in Fig. 13. As in the 2.5 GPa case (Fig. 11), the high-field experiments did not result in significantly different transmitted waveforms. For each shock amplitude, the high-field case shows a slightly more rapid initial rise followed by a slightly slower rise to a common final state.

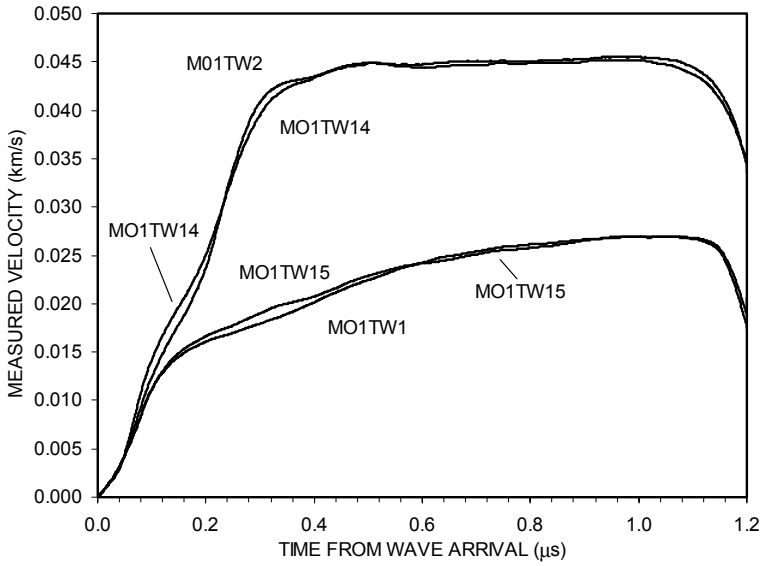

Fig. 13 Field effects on transmitted wave profiles for 1.6 GPa and 0.9 GPa shock inputs.

6. Microstructural Effects in Common-Density Materials

In the present study, four materials prepared through the chemical process had bulk densities that matched that of the baseline material. As described in Section 2, each of these materials had different porous microstructures resulting from the addition of pore formers with different shapes and sizes. The material designated CP1 (with rod-shaped pore formers 5-15 μm in diameter and ≥ 20 μm in length) became available relatively early in the study, and a number of CP1 experiments were conducted under conditions that matched previous experiments with the MO1 baseline material (made with 50-100 μm spherical pore formers). These comparisons examine potential differences resulting from the preparation process, as well as from the very different pore morphologies. Figure 14 shows comparative transmitted-wave profiles from experiments that produced final stresses of 0.9 GPa, 2.5 GPa, and 4.6 GPa in 4.0-mm-thick samples. The

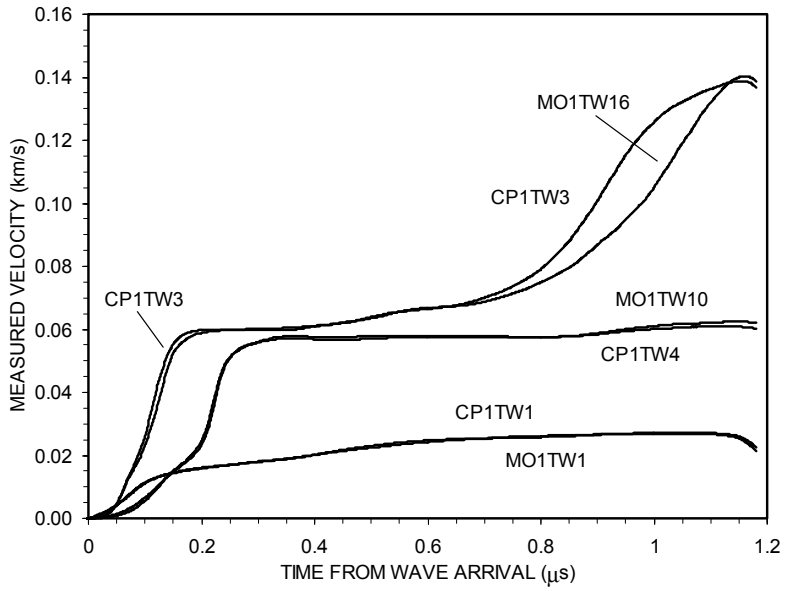

Fig. 14 Comparisons between transmitted wave profiles in common-density materials made using different processes and very dissimilar pore formers.

lower two profiles are from configuration "A" shock-input experiments with short-circuit loads, and show no discernible differences (even if plotted on an expanded scale). At this low amplitude, the wave structure initially reflects some process that results in anomalous compressibility, then the incomplete phase transformation. The intermediate profiles in Fig. 14 are from configuration "C" ramp-input experiments with short-circuit loads. For these

conditions the phase transformation should be complete, and dynamic yielding is not yet apparent. These profiles also show very little difference between the two materials. The upper two profiles are from configuration "C" high-field experiments at a much higher impact velocity, resulting in profiles that reflect the dynamic yielding process. The profile for the CP1 material shows a slightly faster rise to the yielding plateau, and a somewhat steeper rise late in the yielding process. The useful VISAR recording time was not sufficient for these profiles to reach a final Hugoniot state. Overall, the comparisons in Fig. 14 indicate that differences in the two preparation processes and in the two porous microstructures do not have a significant effect on the constitutive mechanical properties that govern transmitted wave profiles, at least up to the onset of dynamic yielding.

The next three figures compare depoling currents generated in MO1 experiments with currents recorded in matching CP1 experiments. The CP1 samples were slightly shorter in the electrode dimension perpendicular to the shock motion (25 mm instead of 28 mm), and measured currents from CP1 samples were scaled by the ratio of these numbers according to Eq. (1). Figure 15 shows currents resulting from 0.9 GPa shock inputs under both short-circuit (10Ω load) and high-field (1150Ω load) conditions. Figure 16 shows currents resulting from 2.5 GPa ramp inputs under both short-circuit and high-field conditions. Finally, Fig. 17 shows currents resulting from 4.6 GPa ramp inputs under high-field conditions. It should be noted that several

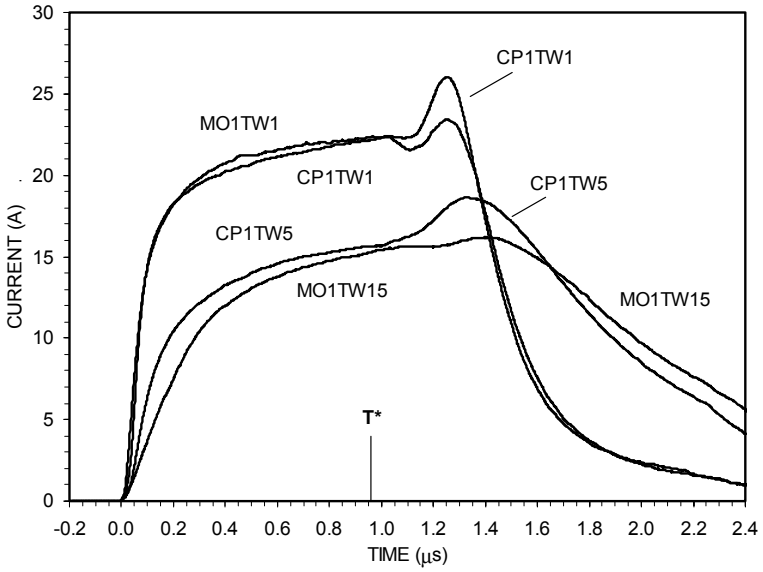

Fig. 15 Comparison of currents generated by 0.9 GPa shock inputs in common-density materials under both short-circuit and high-field conditions.

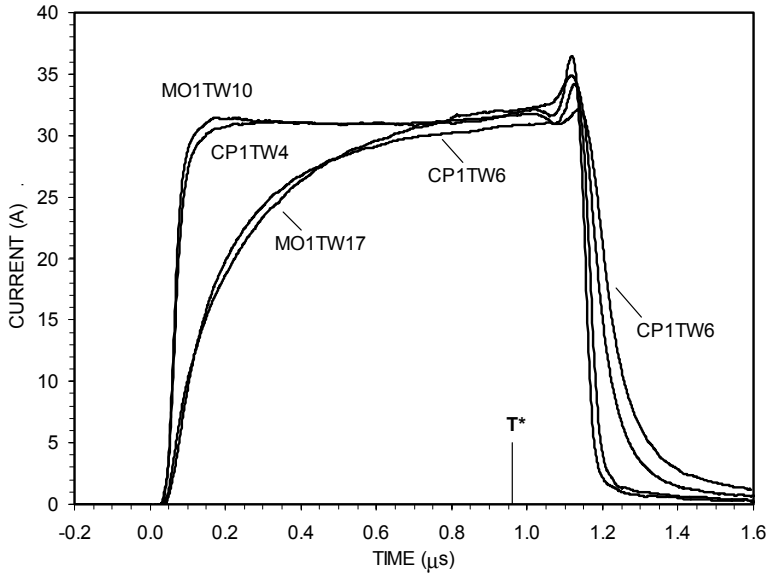

Fig. 16 Comparison of currents generated by 2.5 GPa ramp inputs in common-density materials under both short-circuit and high-field conditions.

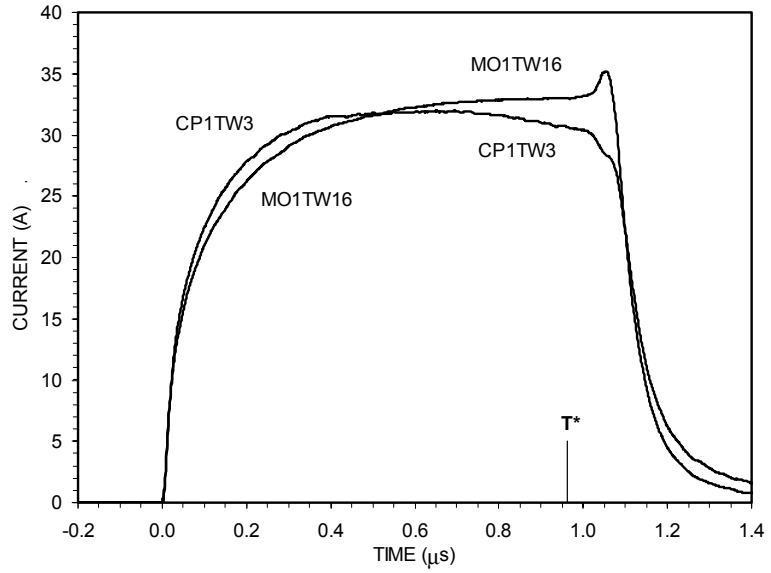

Fig. 17 Comparison of currents generated by 4.6 GPa ramp inputs into common-density materials under high-field conditions.

early attempts to introduce 4.6 GPa shock inputs into MO1 samples under high-field conditions resulted in high-voltage breakdowns, and this condition was not attempted with the other materials. The comparisons in Figs. 15-17 do not show substantial differences between the two materials. Small variations in generated currents are seen in repeat experiments on the same

material, primarily due to small differences in remanent polarization, and the differences seen in these figures are comparable to those variations. A possible exception can be seen in the high-field cases at 2.5 GPa and 4.6 GPa, where the CP1 currents appear to be falling off late in time.

The common-density materials prepared chemically using spherical pore formers of various sizes, CP4-CP6, became available later during the course of the present study. Again, experiments were conducted with these materials under conditions that matched previous experiments with the baseline material. Figure 18 shows transmitted-wave profiles recorded in 4.5 GPa shock experiments (configuration "A") under short-circuit load conditions. The first

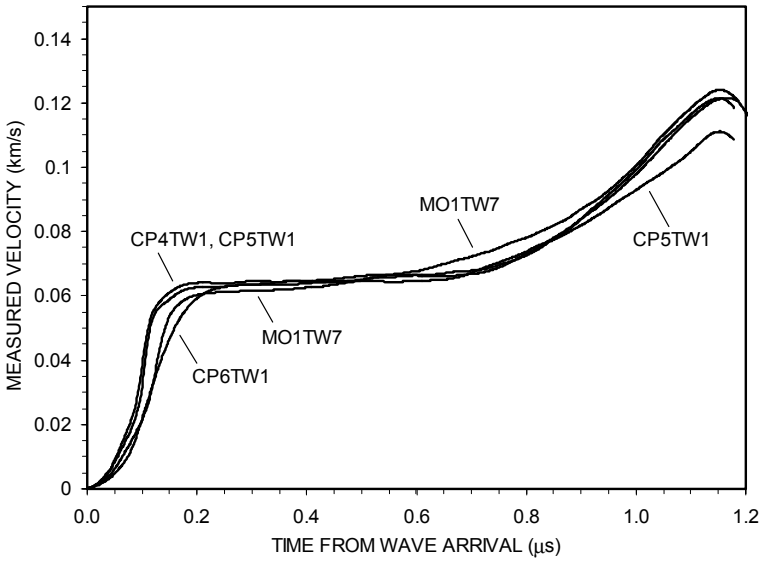

Fig. 18 Comparisons between transmitted wave profiles from 4.5 GPa shock inputs in common-density materials made with different spherical pore formers.

two materials (CP4 and CP5, made with 15 μm and 80 μm pore formers, respectively) show a more rapid rise to the plateau level corresponding to the onset of dynamic yielding. These two materials and CP6 (140 μm pore formers) show a very consistent threshold for yielding that appears to be slightly higher than for MO1. Following the plateau, small differences appear as the profiles rise towards final Hugoniot states. Figure 19 shows the depoling currents recorded in the same experiments. The CP4 and CP5 currents essentially overlap, with strong initial overshoots as the sharp input shocks enter the samples. Steady current levels are very close for the four cases. Slight differences in the T* values are indicated, as the CP4-CP6 materials have slightly higher acoustic velocities than the MO1 material. Figure 20 shows one final comparison

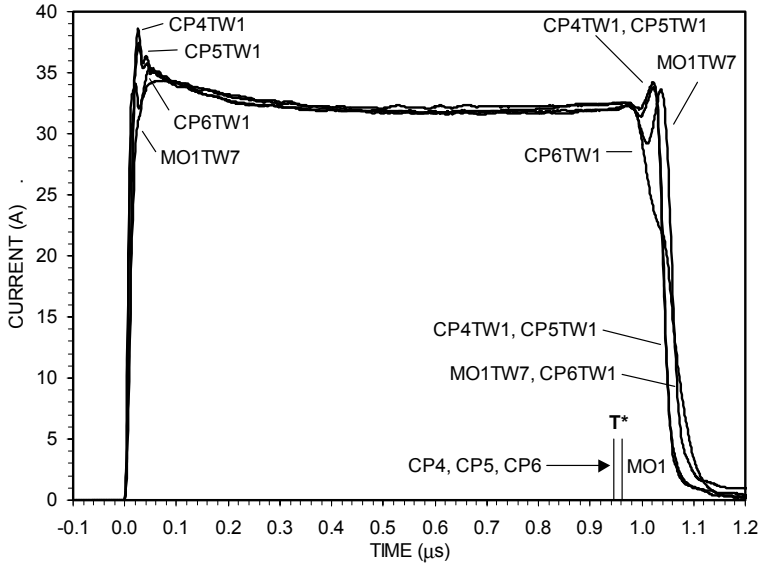

Fig. 19 Comparison of short-circuit currents generated by 4.6 GPa shock inputs into common-density materials.

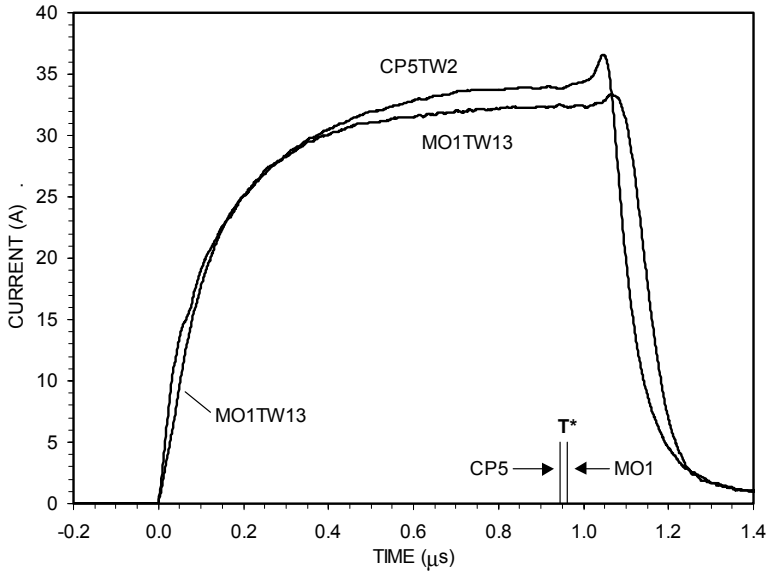

Fig. 20 Comparison of currents generated by 2.5 GPa shock inputs into common-density materials under high-field conditions.

between depoling currents generated by 2.5 GPa shock inputs under high-field conditions. Compared to the MO1 case, the CP5 experiment showed a higher final current level and an earlier fall after wave transit. Although impact velocities were within 1%, the current profiles suggest that the wave velocity was higher within this CP5 sample.

7. Initial Density Effects

A number of materials were used in the present study to investigate the effects of differences in initial density. Two chemically prepared materials, CP2 and CP3, were made with different amounts of the small, rod-shaped pore former used in the CP1 material. Resulting bulk densities were 3.7% higher and 4.8% lower than the baseline density, respectively. In addition, the mixed oxide material MO2 was made without pore formers, resulting in a bulk density 5.0% higher than baseline. Only unpoled discs of this material were available, however. As discussed in Section 3, limited reverse-impact experiments were conducted with these materials to provide comparisons with the baseline Hugoniot curve (Fig. 4). The extensive number of experiments required to establish a complete Hugoniot curve for each material was beyond the scope of this study. Consequently, comparative experiments where predicted peak stresses are matched (as in the common-density experiments) were not pursued. Instead, comparative experiments were conducted at fixed impact conditions, recognizing that the resulting peak stresses would vary between different materials.

Figure 21 shows transmitted-wave profiles from configuration "C" (ramp input) experiments under short-circuit conditions. Impact velocities were 0.406 ± 0.002 km/s, resulting in a peak stress of 2.54 GPa in the baseline-density CP1 sample. Peak stresses were approximately 2.6-2.7 GPa and 2.3-2.4 GPa in the CP2 and CP3 cases, respectively. The low-density CP3 case shows

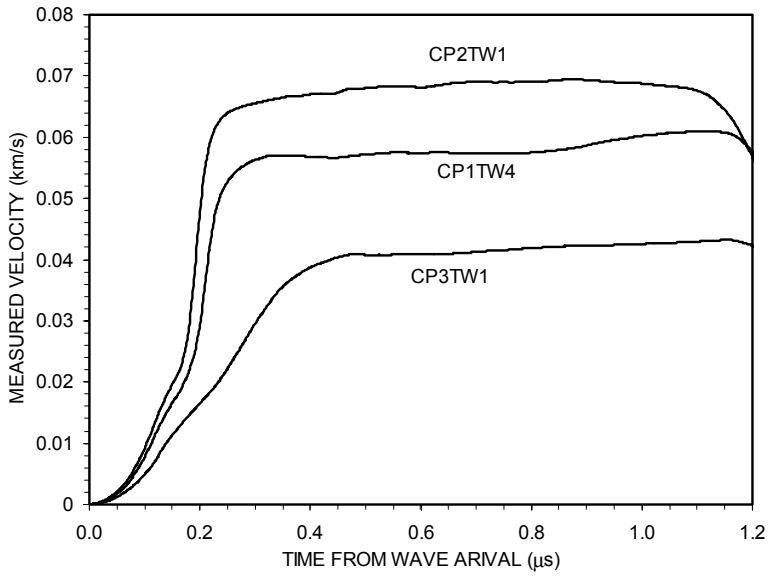

Fig. 21 Transmitted wave profiles in different density samples produced by a fixed impact condition (resulting in a 2.5 GPa ramp input for CP1).

a more extended wave structure than the other two cases. The large differences in the final velocity values are seemingly inconsistent with estimates from the limited Hugoniot data (Fig. 4) and the fact that initial densities vary by less than ± 5%. As will be shown in a subsequent figure, the impact conditions produced states that were above the thresholds for dynamic yielding in the CP1 and CP3 cases. The steady velocity in each of these cases is actually the yielding plateau (Fig. 7), with the eventual rise towards a Hugoniot state not occurring within the available recording time.

The depoling currents recorded in these experiments are shown in Fig. 22. Differences in current levels also appear to be quite large, with the CP3 case showing late depoling due to the

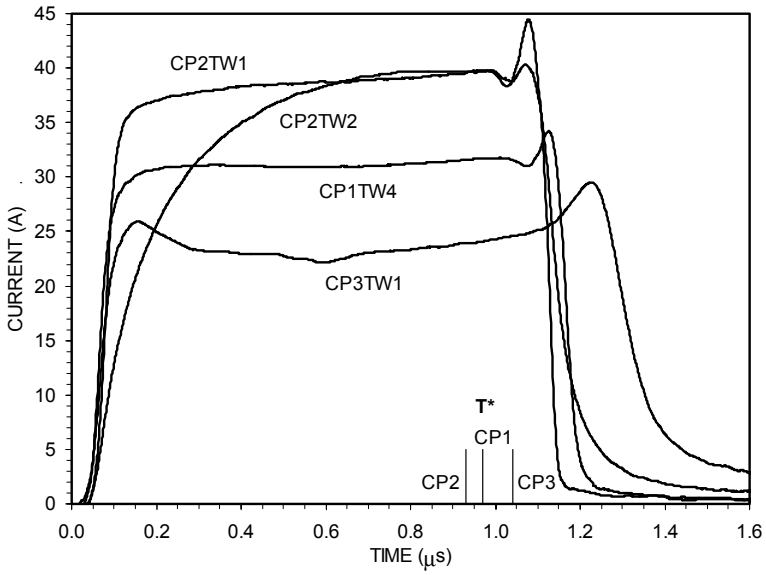

Fig. 22 Currents generated in different density samples under fixed impact conditions (same as Fig. 21).

more extended wave structure (and possibly incomplete depoling during the initial wave transit). Differences in the T* values reflect the fact that acoustic velocities for the CP2 and CP3 materials are 4.3% higher and 6.6% lower, respectively, than for the CP1 material (Table 2). The total charge release in these experiments is found from the time integral of the current histories, and provides a measure of the initial polarization if depolarization is complete. Integrating over sufficient time to account for late wave interactions, the values found for the CP2, CP1, and CP3 cases are 35.3, 30.0, and 26.8 $\mu C/cm^2$, respectively. These values can be used with Eq. (1) to estimate average current levels during shock transit that are consistent with the curves in Fig. 22. The necessary wave velocities for the CP1 and CP3 cases, however,

correspond to the yielding states rather than the final Hugoniot states. Also shown in Fig. 22 is a matching high-field (1150Ω load) experiment conducted with the high-density CP2 material. The peak field reached in this experiment, 40.3 kV/cm, was the highest achieved during the present study.

The polarization values found from the current histories drop more rapidly with initial density than the linear dependence that would be expected if remanent polarization simply scaled with density. In hydrostatic depoling experiments on similar PZT 95/5-2Nb materials, Tuttle et al.[35] found that phase transition characteristics changed significantly with initial density. As sample density decreased, the pressure at the onset of the transition decreased and the total change in pressure to complete the transition increased. The total released charge decreased more rapidly than linearly with decreasing density, as found in the present experiments.

To examine density effects on dynamic yielding characteristics systematically, a set of configuration "B" (shock input) experiments were conducted with different unpoled materials at an impact velocity of 0.620 ± 0.002 km/s. This impact condition produced a peak stress of 4.53 GPa in the baseline-density CP1 sample, and peak stresses that varied from approximately 4.0 GPa to 5.2 GPa in the other materials. As seen in Fig. 23, the resulting transmitted-wave profiles have very large differences. The profile rise time prior to the yielding threshold increases

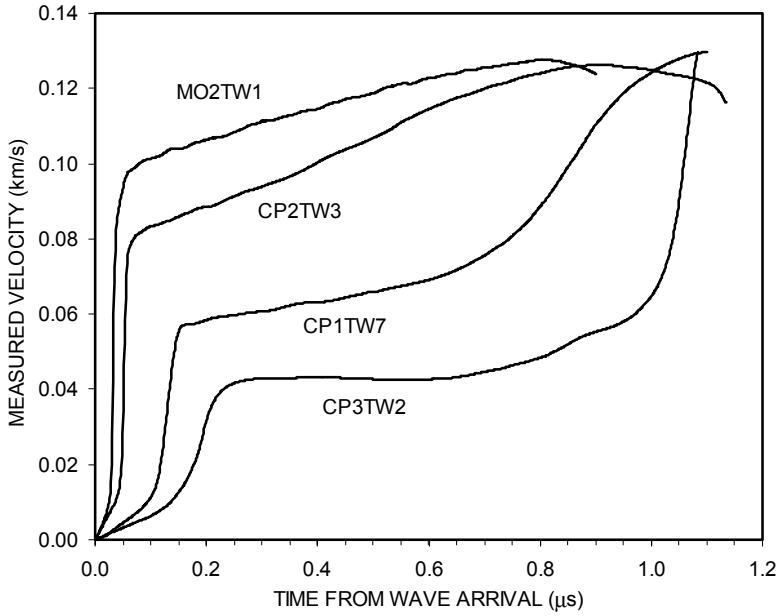

Fig. 23 Transmitted wave profiles in different density samples produced by a fixed impact condition (resulting in a 4.5 GPa shock input for CP1).

rapidly with decreasing density, while the measured velocities corresponding to the yielding thresholds change by more than a factor of two. In addition, the wave structure following the yielding threshold shows a strong dependence on density. For the highest density case, a gradual velocity rise begins immediately. As initial density is decreased, a slower initial rise is followed by a more rapid late-time rise, giving the wave profile a more distinct multi-wave structure. The large differences in these yielding profiles suggest that the dominant yielding mechanism may vary with initial density.

The wave profiles in Fig. 23 can be used to obtain stress thresholds for dynamic yielding. For materials at the baseline density, the Hugoniot curve established in reverse-impact experiments (Fig. 4) can be used to determine the stress at the yielding threshold. For the other materials, the more limited Hugoniot states that were measured can be used to estimate the yielding stresses. The resulting values for the different initial densities are shown in Fig. 24. Also shown in this figure are yielding data from the early study by Doran,[7] in which PZT 95/5-1Nb material was hot-pressed to achieve higher densities. Although this was a slightly different composition, the collective data appear to be self-consistent and support the general conclusion that the threshold for dynamic yielding can vary by a factor of three over the range of initial densities that can be achieved in this material.

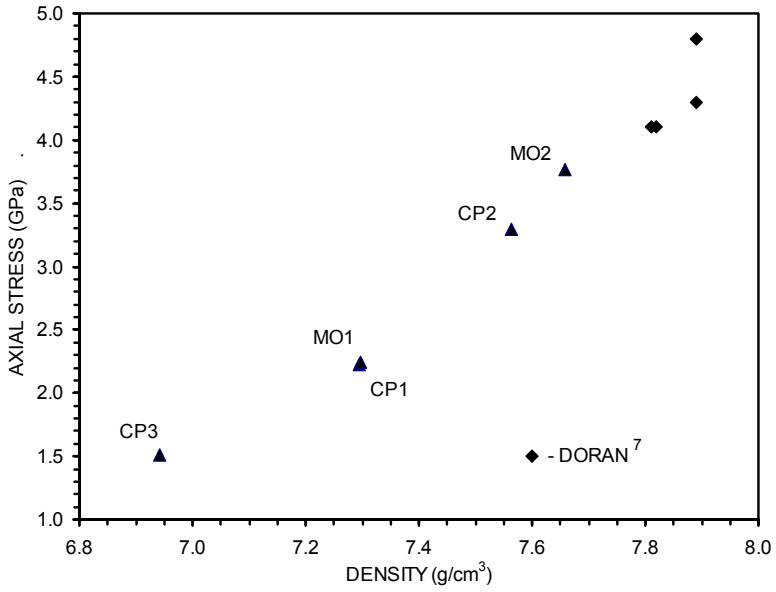

Fig. 24 Threshold stress for the onset of dynamic yielding as a function of initial density.

8. Summary

Extensive experiments in a previous study established detailed shock properties for the baseline MO1 material. The collective results identified a complex material behavior governed by anomalous compressibility and incomplete phase transformation at low shock amplitudes, and a slow yielding process at high shock amplitudes. Depoling depoling currents are reduced at low shock stresses due to the incomplete transformation, and are reduced further in the presence of a strong electrical field. Experiments using input waves with finite rise times ("ramp waves") showed that transformation kinetics were dependent on the wave structure as well as the final stress. At high shock stresses, depoling currents are driven by a wave structure governed by the threshold for dynamic yielding. This wave structure is insensitive to the final wave amplitude, resulting in depoling currents that do not increase with shock amplitude for stresses above the yield threshold.

In the present study, the effects of microstructural differences on this complex behavior were investigated. By varying the type and quantity of pore formers added during material processing, materials were made having different porous microstructures both at the baseline density and at different densities. Limited reverse-impact experiments were conducted to provide comparative Hugoniot states. These results indicated that the Hugoniot curve is not sensitive to differences in the porous microstructure in common-density materials, but steepens rapidly with increasing initial density. In transmitted-wave experiments, experimental conditions were matched to previous experiments with the baseline material to provide direct comparisons. Transmitted waveforms and corresponding depoling currents were obtained for both shock and ramp wave inputs over a range of shock conditions. Most experiments compared materials having the same density as the baseline material. The chemically prepared material CP1, available relatively early during this study, showed essentially no differences in transmitted waveforms compared to MO1 material for stresses up to onset of yielding, and possibly small differences during the yielding process. Corresponding depoling currents also matched closely, except possibly under high-stress, high-field conditions. The more recent materials CP4-CP6 also showed profiles and currents that matched MO1 experiments, although possibly not as closely as the CP1 material. Acoustic velocities were consistently higher in these materials, and one high-field experiment produced currents that suggested a higher shock velocity. Only subtle differences between these chemically prepared materials were seen in the recorded waveforms and currents.

One mixed oxide material and two chemically prepared materials having non-baseline densities were available during the course of this study. Densities in these materials ranged from 6.94 g/cm^3 to 7.66 g/cm^3, corresponding to porosity values from 13.2% to 4.3%. Although these densities are within ± 5% of the baseline value, experiments on normally poled samples showed large differences in both transmitted waveforms and depoling currents. Average currents decreased rapidly with decreasing density, largely due to initial polarization values that decreased more rapidly than linearly with initial density. Unexpectedly large differences in waveforms were due to the onset of dynamic yielding in some materials. Density effects on yielding characteristics were examined more carefully in a series of high-stress, shock input experiments on unpoled samples. These experiments showed that waveform rise time prior to the onset of yielding increased rapidly with decreasing density, while the measured velocities corresponding to yielding thresholds changed by more than a factor of two. The wave structure following yielding also changed significantly with density, suggesting that the dominant yielding mechanism could be changing.

In summary, only subtle changes in shock behavior were seen in common-density materials having different porous microstructures, whereas profound changes were observed when initial density was varied. Increasing the initial density results in both a higher initial polarization and a higher threshold stress for dynamic yielding, which governs the wave structure that drives the phase transformation. As a result, depoling currents produced by a given impact condition increase rapidly with initial density. The density sensitivity of the yielding threshold could also have significance in terms of the shock response under high-field conditions. Intuitively, failure mechanisms associated with yielding in ceramic materials could result in adverse changes to dielectric properties. These observations and considerations indicate why densities should not be too low, but fail to reveal why early studies found that densities should not be too high. In terms of power supply applications, a basic conclusion from the present study is that the choice of pore former used in material processing is not as significant as careful optimization of the initial density. To this end, additional studies into the shock response of high-density materials may be required.

References

1. B. Jaffe, W. R. Cook, Jr., and H. Jaffe, Piezoelectric Ceramics (Academic Press, London, 1971).

2. M. J. Haun, E. Furman, S. J. Jang, and L. E. Cross, Ferroelectrics **99**, 13 (1989).

3. F. W. Neilson, Bull. Am. Phys. Soc. **2**, 302 (1957).

4. F. Bauer and K. Vollrath, Ferroelectrics 12, 153 (1976)

5. R. K. Linde, J. Appl. Phys. 38, 4839 (1967).

6. W. J. Halpin, J. Appl. Phys. **37**, 153 (1966).

7. D. G. Doran, J. Appl. Phys. **39**, 40 (1968).

8. I. J. Fritz and J. D. Keck, J. Phys. Chem. Solids **39**, 1163 (1978).

9. I. J. Fritz, J. Appl. Phys. **49**, 4922 (1978).

10. W. J. Halpin, J. Appl. Phys. **39**, 3821 (1968).

11. P. C. Lysne and C. M. Percival, J. Appl. Phys. **46**, 1519 (1975).

12. P. C. Lysne, J. Appl. Phys. **48**, 1020 (1977).

13. P. C. Lysne, J. Appl. Phys. **48**, 4565-4568 (1977).

14. P. C. Lysne, "Electrical Response of Shock-Wave-Compressed Ferroelectrics," in High Pressure Science and Technology, Vol. I, edited by K. D. Timmerhaus and M. S. Barber, Plenum Press, New York, 1978, pp. 202-209.

15. J. J. Dick and J. E. Vorthman, J. Appl. Phys. **49**, 2494 (1978).

16. L. C. Chhabildas, "Dynamic Shock Studies of PZT 95/5 Ferroelectric Ceramic," Sandia National Laboratories Report SAND84-1729 (1984).

17. L. C. Chhabildas, M. J. Carr, S. C. Kunz, and B. Morosin, "Shock Recovery Experiments on PZT 95/5," in Shock Waves in Condensed Matter, edited by Y. M. Gupta (Plenum Press, New York, 1986) pp. 785-790.

18. L. J. Storz and R. H. Dungan, "A Study of the Electrical, Mechanical, and Microstructural Properties of 95/5 PZT as a Function of Pore Former Type and Concentration," Sandia

National Laboratories Report SAND85-1612 (1986). Note: this report is Specified External Distribution Only.

19. R. E. Setchell, L. C. Chhabildas, M. D. Furnish, S. T. Montgomery, and G. T. Holman, "Dynamic Electromechanical Characterization of the Ferroelectric Ceramic PZT 95/5," in Shock Compression of Condensed Matter – 1997, edited by S. C. Schmidt et al., AIP Conference Proceedings 429, New York, 1998, pp. 781-784.

20. R. E. Setchell, S. T. Montgomery, L. C. Chhabildas, and M. D. Furnish, "The Effects of Shock Stress and Field Strength on Shock-Induced Depoling of Normally Poled PZT 95/5," in Shock Compression of Condensed Matter – 1999, edited by M. D. Furnish et al., AIP Conference Proceedings 505, New York, 2000, pp. 979-982.

21. M. D. Furnish, L. C. Chhabildas, R. E. Setchell, and S. T. Montgomery, "Dynamic Electromechanical Characterization of Axially Poled PZT 95/5," in Shock Compression of Condensed Matter – 1999, edited by M. D. Furnish et al., AIP Conference Proceedings 505, New York, 2000, pp. 975-978.

22. S. T. Montgomery, R. M. Brannon, J. Robbins, R. E. Setchell, and D. H. Zeuch, "Simulation of the Effects of Shock Stress and Electrical Field Strength on Shock-Induced Depoling of Normally Poled PZT 95/5," in Shock Compression of Condensed Matter – 2001, edited by M. D. Furnish et al., AIP Conference Proceedings 620, New York, 2002, pp. 201-204.

23. R. E. Setchell, "Recent Progress in Understanding the Shock Response of Ferroelectric Ceramics," in Shock Compression of Condensed Matter – 2001, edited by M. D. Furnish et al., AIP Conference Proceedings 620, New York, 2002, pp. 191-196.

24. R. H. Dungan and L. J. Storz, J. Am. Ceram. Soc. **68**, 530 (1985).

25. J. A. Voigt, D. L. Sipola, B. A. Tuttle, and M. Anderson, U.S. Patent No. 5,908,802, June 1, 1999.

26. J. H. Gieske, Sandia National Laboratories, private communication

27. Ya. B. Zel'dovich and Yu. P. Raizer, Physics of Shock Waves and High-Temperature Hydrodynamic Phenomena, Vol. II, edited by W. D. Hayes and R. F. Probstein (Academic Press, New York, 1966), pp.705-731.

28. L.M. Barker and R.E. Hollenbach, J. Appl. Phys. **43**, 4669 (1972).

29. R. E. Setchell, J. Appl. Phys. **91**, 2833 (2002).

30. R.E. Setchell, J. Appl. Phys. **50**, 8186 (1979).

31. L.M. Barker and R. E. Hollenbach, J. Appl. Phys. **41**, 4208 (1970).

32. R. A. Graham and W. P. Brooks, J. Phys. Chem. Solids **32**, 2311 (1971).

33. M. U. Anderson, R. E. Setchell, and D. E. Cox, "Shock and Release Behavior of Filled and Unfilled Epoxies," in Shock Compression of Condensed Matter – 1999, edited by M. D. Furnish, L. C. Chhabildas, and R. S. Hixson (American Institute of Physics, CP505, Melville, N.Y., 2000) p. 551.

34. P. C. Lysne and L. C. Bartel, J. Appl. Phys. **46**, 222 (1975).

35. B. A. Tuttle, P. Yang, J. H. Gieske, J. A. Voigt, T. W. Scofield, D. H. Zeuch, and W. R. Olson, J. Am. Ceram. Soc. **84**, 1260 (2001).

Appendix A

Influence of Microstructure on the Ferroelectric-Antiferroelectric Transition and Pressure-Temperature Phase Diagram of Chem-Prep PZT 95/5: Porosity Effects

Eugene L. Venturini, George A. Samara, Bruce A. Tuttle and James A. Voigt

Motivation

The influence of microstructure on the properties and phase behavior of ferroelectric ceramics is a subject of considerable scientific and technological importance. Of special interest in the present project are the influences of porosity (or density) and type of pore former (Lucite vs. Avicel) on the various phase boundaries, particularly the pressure-induced rhombohedral ferroelectric (F_{R1}) – to – orthorhombic antiferroelectric (A_o) phase transition, in Chem-Prep PZT 95/5 with 2 at.% Nb. This transition forms the basis of shock-actuated pulse power sources used in NW applications. Although in the devices the transition is induced by shock compression, which results in depoling of the PZT 95/5 elements and the release of bound charge, it has always proven to be important and necessary to complement the shock studies with static high-pressure results. Shock experiments are very expensive and time consuming, making it prohibitive to determine complex phase diagrams such as that of PZT 95/5 by shock compression. Static high-pressure techniques allow us to determine such phase diagrams more quickly and at a much lower cost. Although the stress states achieved by hydrostatic compression are different from those reached by shock compression, the differences can be taken into account, and the static results provide a good definition of the phase diagram that guides the planning and interpretation of shock results. In this regard it is worth emphasizing that although at ambient and low temperatures the F_{R1} – to - A_o transition is the primary mechanism for charge release, at the high end of the STS temperature range it is certain that the initial shock amplitude will take the PZT into other regions of its phase diagram. Thus, knowledge of details of the phase diagram is necessary.

Accomplishments

We are investigating the influence of porosity and pore formers on the phase diagram of PZT 95/5. The phase boundaries are determined from anomalies in the dielectric constant, $\in'$,

and/or dielectric loss, tan δ, measured as functions of temperature, hydrostatic pressure and frequency. Chem-Prep samples with densities ranging from 7.3 to 7.8 g/cm^3 and with both Lucite and Avicel pore formers have been investigated and the results compared. For one density (7.3 g/cm^3), Chem-Prep results were compared with results on mixed oxide material of the same density. Table 1 provides a description of the samples investigated.

Figure 1 shows the isothermal dependence of $\in'$ at three temperatures for a 7.3 g/cm^3 Chem-Prep sample (HF803 PZT) where Lucite was the pore former. The sharp drop in $\in'$ at ~ 2.2 kbar at 300 K is the signature of the F_{R1} – to - A_o transition. The sharpness of the transition is unusual for a ceramic and attests to high quality of the sample. We note that for Avicel samples of the same density, the transition is much broader requiring 0.4 – 0.5 kbar for completion. The results in Fig. 1 clearly show that the transition pressure increases with increasing temperature.

Figure 2 shows the temperature dependence of the F_{R1} – to - A_o transition pressure, or the F_{R1} – to - A_o phase boundary, for four different samples of the same 7.3 g/cm^3 density: two chem.-prep samples with Avicel pore former (HF631 and HF635), a Chem-Prep sample with Lucite spheres (HF803) and a mixed oxide sample with Lucite spheres (HF453). The results clearly show that, within experimental uncertainty, all samples exhibit the same phase boundary implying that sample density is the dominant factor in determining the transition pressure under hydrostatic compression. This is found to be true under shock compression also, as discussed in the present report.

Figure 3 shows the large influence of sample density on the F_{R1} – to - A_o phase boundary for samples having Avicel as the pore former. With the exception of the sample with no Avicel, the results show a large decrease of transition pressure with decreasing density. It is not clear why the Avicel-free sample does not obey the trend in the other data. For the other samples, the decrease of transition pressure with decreasing density (increasing porosity) is most likely due to the availability of open volume (porosity), making it easier for the rhombohedral to orthorhombic distortion to take place.

One of the characteristics of the F_{R1} – to - A_o transition is the irreversibility of the transition at and below room temperature. On releasing pressure the sample remains in the A_o phase. To recover the F_{R1} phase it is necessary to heat the sample at a reduced pressure, which transforms it into the higher temperature modification of F_{R1}, which is F_{R2}. Subsequent cooling

of F_{R2} at 1 bar reverts the sample back to F_{R1}. The F_{R2} – to - F_{R1} transformation is accompanied by counter rotations of adjacent oxygen octehedra of the pervoskite lattice. Such rotations are non-polar.

Figure 4 shows the dielectric signatures of the A_o – to – F_{R2} transition at 1 and 2 kbar and of the A_o-to-A_T transition at 3 and 4 kbar for HF803. The inset in Fig. 4 shows the two-phase boundaries.

Figure 5 shows a tentative temperature-pressure phase diagram for Chem-Prep PZT 95/5 (2%Nb) for a density of 7.3 g/cm^3. The solid lines are the phase boundaries based on actual measurements from various samples of this density, and the dashed lines are the expected phase boundaries based on analogy with the phase diagram for the mixed oxide PZT 95/5. Unfortunately, the available resources did not allow us to complete this phase diagram, something that we plan to do.

Concluding Remarks

Although research investigating the influence of changes in the composition on the response of Chem-Prep PZT 95/5 in shock-actuated devices is continuing, there is a good likelihood that the material will be close to the 7.3 g/cm^3 materials investigated in the present work. Thus, it will be necessary to complete the phase diagram in Fig. 5. Of particular interest will be the region between 320 - 400 K and 1 - 3 kbar where various phases meet. This mixed phase region will have a strong influence on shock propagation, and, thereby, on the operation of the device at the high temperature end.

This work should also be extended to include the influence of biasing electric fields of the various phase boundaries and thereby determine the combined influences of pressure and field on the phase diagram. This is important because in actual operation the devices are exposed to a combination of pressure and electric fields. Special emphasis will be on the behavior of the FE/AFE phase boundary at both high and low temperatures (covering the STS temperature range), but also needed is investigation of the boundaries of phases that may be visited in the early part of the shock loading, i.e., the very high pressure end. Thus, the outcome will be a complete description of the phase behavior of this PZT as functions of pressure, temperature and electric field. It is also desirable to investigate the dielectric permittivity and dielectric losses of the material over this range of variables, needed information for the design and modeling of components.

Table 1. Designations and descriptions of the PZT 95/5 (2% Nb) samples investigated.

Designation	Density	Method of Synthesis	Pore Former
HF803	7.3 g/cm^3	Chem.-prep	Lucite
HF631	7.3	Chem.-prep	Avicel
HF635	7.3	Chem.-prep	Avicel
HF453	7.3	Mixed oxide	Lucite
SP16C-16	7.8	Chem.-prep	None
SP16C-16	7.7	Chem.-prep	Avicel
SP16C-16	7.6	Chem.-prep	Avicel
SP16C-16	7.4	Chem.-prep	Avicel

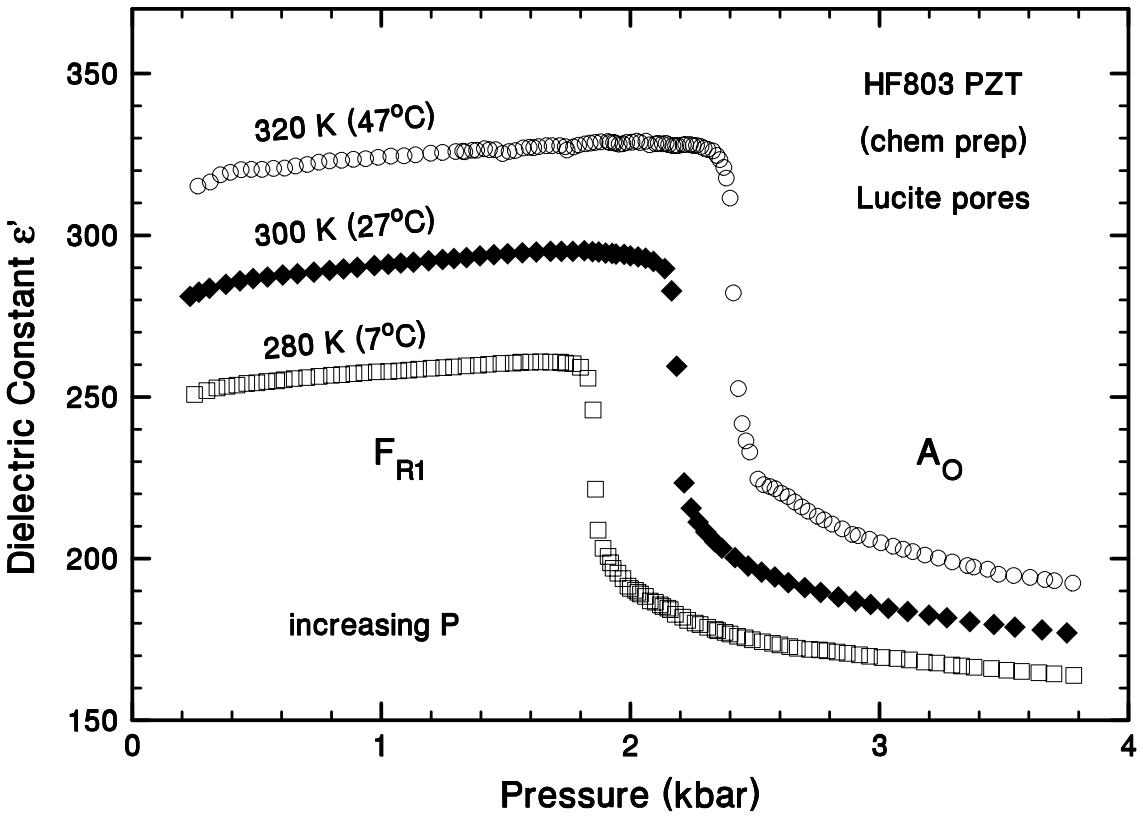

Fig. 1 Isothermal pressure dependence of the dielectric constant of HF803 PZT showing the increase of the $F_{R1} \rightarrow$ Ao transition pressure with increasing temperature.

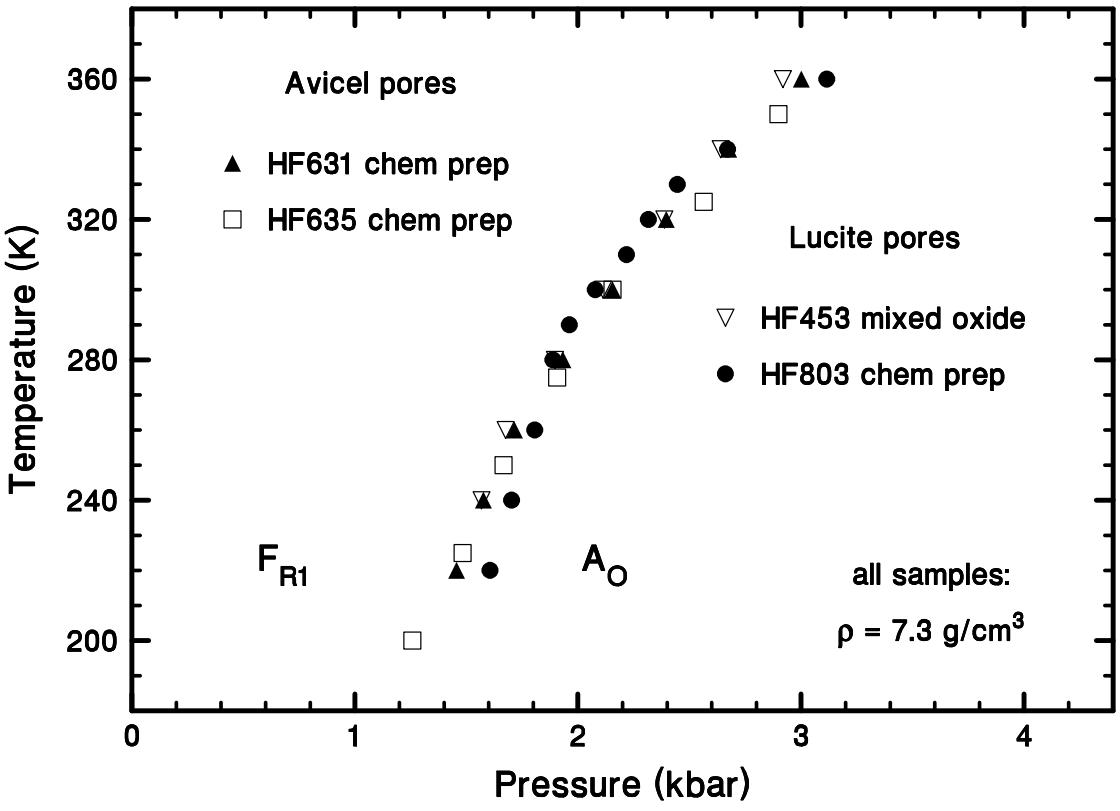

Fig. 2 The $F_{R1} \rightarrow A_o$ phase boundary for several PZT 95/5 samples having the same density (7.3g/cm^3).

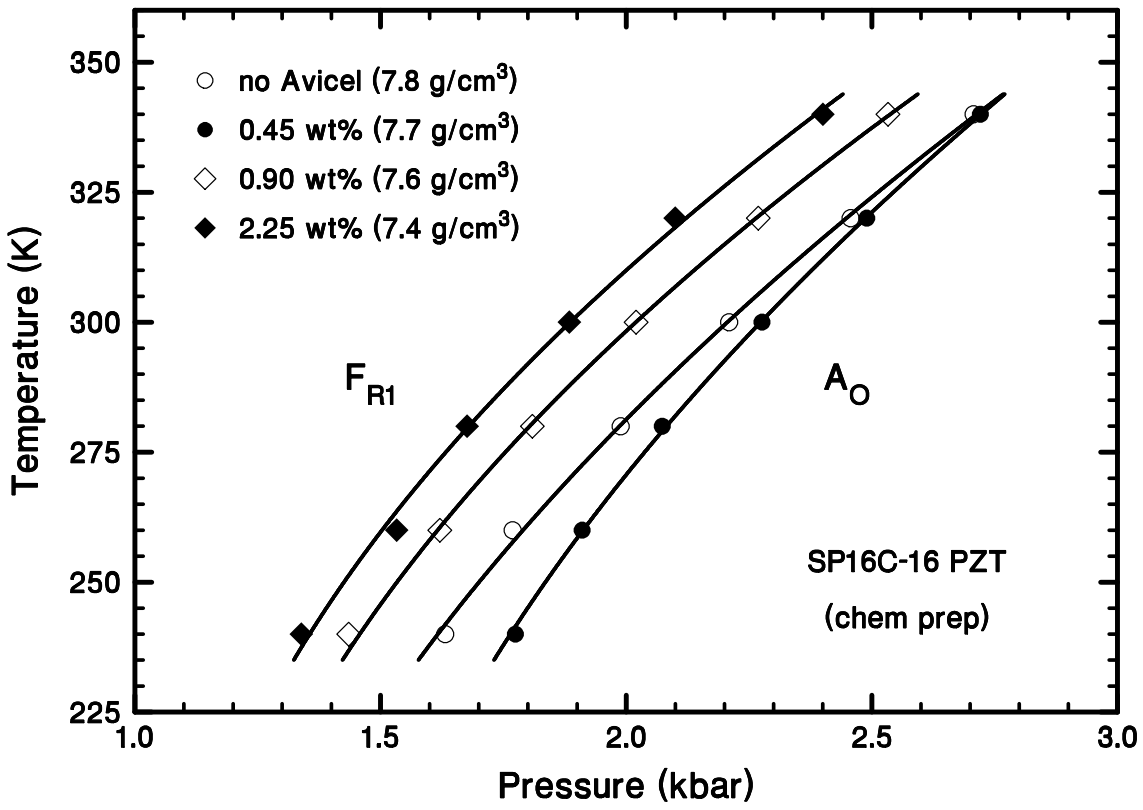

Fig. 3 The strong influence of density on the $F_{R1} \rightarrow A_o$ phase boundary for PZT 95/5.

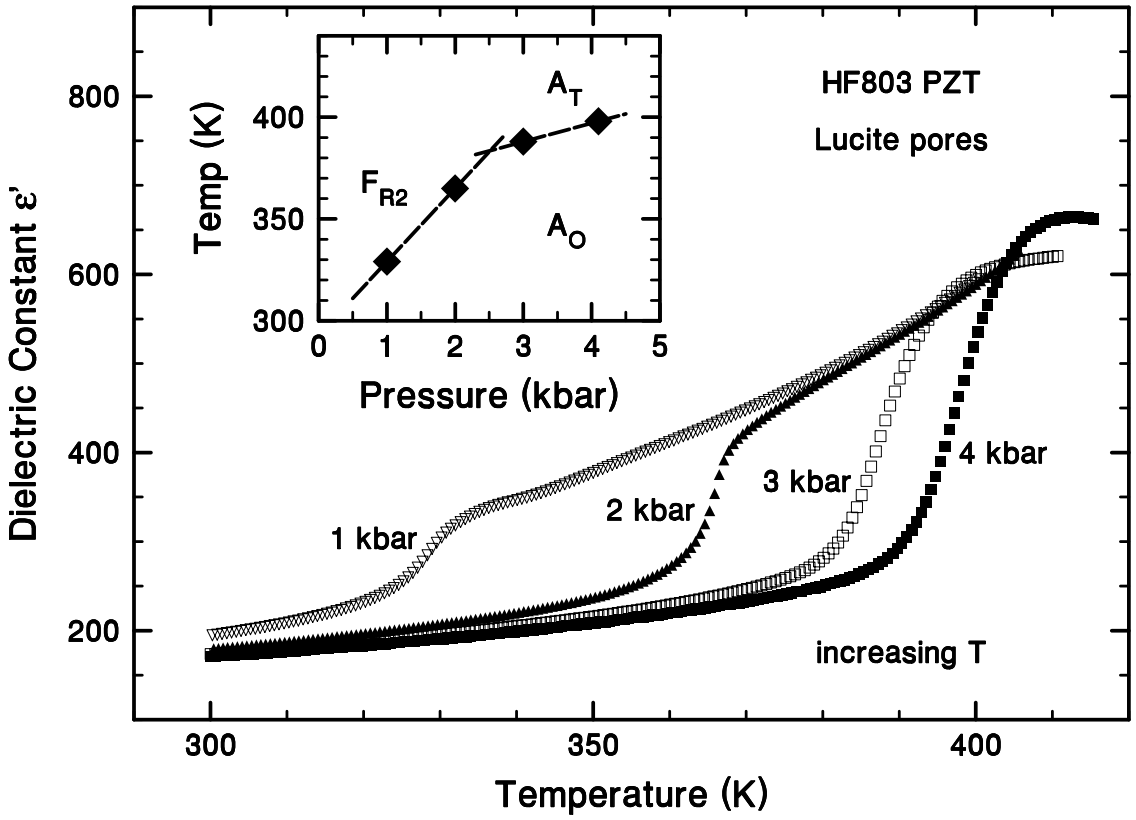

Fig. 4 The dielectric signatures of the $A_o \rightarrow F_{R2}$ (1 and 2 kbar) and $A_o \rightarrow A_T$ (3 and 4 kbar) transitions with increasing temperature.

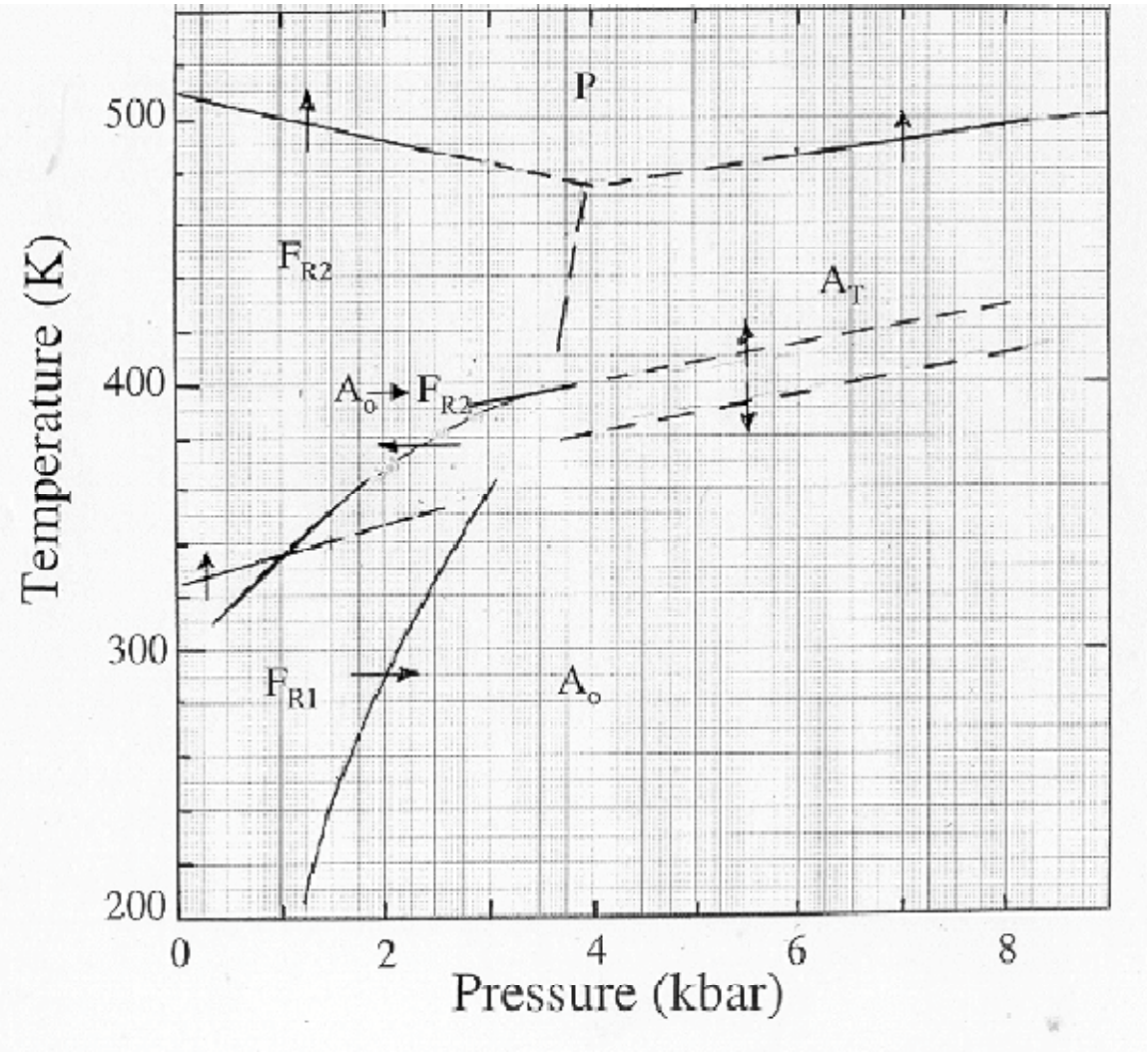

Fig. 5 Tentative Temperature-Pressure phase diagram for PZT 95/5 (2% Nb) at density of 7.3g/cm^3.

Appendix B

Publications Resulting from this Project (to date)

1) R. E. Setchell, B. A. Tuttle, J. A. Voigt, and E. L. Venturini, "Effects of Initial Porosity on the Shock Response of Normally Poled PZT 95/5," in Shock Compression of Condensed Matter – 2001, edited by M. D. Furnish et al., AIP Conference Proceedings 620, New York, 2002, pp. 209-212.

2) R. E. Setchell, "Shock Wave Compression of the Ferroelectric Ceramic PZT 95/5-2Nb: Hugoniot States and Constitutive Mechanical Properties," accepted for publication in the Journal of Applied Physics (2003).

Distribution

1	MS-0188	LDRD Office, 1011
1	MS-0316	J. B. Aidun, 9235
1	MS-0515	S. G. Barnhart, 2561
1	MS-0515	T. A. Haverlock, 2561
1	MS-0515	J. D. Keck, 2561
1	MS-0521	F. M. Bacon, 2502
1	MS-0521	S. T. Montgomery, 2561
1	MS-0521	T. W. Scofield, 2561
1	MS-6117	R. M. Brannon, 6117
1	MS-0819	J. Robbins, 9231
1	MS-0835	E. A. Boucheron, 9141
1	MS-0885	D. B. Dimos, 1801
1	MS-0959	R. H. Moore, 14192
1	MS-0959	P. Yang, 14192
1	MS-1168	M. D. Furnish, 1647
1	MS-1181	L. C. Chhabildas, 1647
1	MS-1181	J.-P. Davis, 1646
1	MS-1181	M. D. Knudson, 1646
1	MS-1186	R. J. Lawrence, 1674
1	MS-1349	W. F. Hammetter, 1843
1	MS-1411	B. G. Potter Jr., 1846
1	MS-1411	B. A. Tuttle, 1843
1	MS-1411	J. A. Voigt, 1846
1	MS-1415	W. B. Gauster, 1110
1	MS-1421	G. A. Samara, 1120
1	MS-1421	M. U. Anderson, 1122
15	MS-1421	R. E. Setchell, 1122
1	MS-1421	E. L. Venturini, 1122
1	MS-1427	J. M. Phillips, 1100
1	MS-9018	Central Technical Files, 8945-1
2	MS-0899	Technical Library, 9616
1	MS-0612	Review & Approval Desk, 9612 for DOE/OSTI